QUANTIFICATION OF THE OCEANOGRAPHIC CONTRIBUTORS TO TIME-VARIANCE IN THE UNDERWATER ACOUSTIC CHANNEL DURING THE DALCOMMS1 EXPERIMENT

by

Maxime Miron-Morin

Submitted in partial fulfillment of the requirements
for the degree of Master of Science

at

Dalhousie University
Halifax, Nova Scotia
November 2018

Table of Contents

List of Tables

List of Figures

List of Abbreviations and Symbols Used

Roman symbol	Description	Units
A	UNESCO Sound speed equation coefficient	
A_1, A_2, A_3	Francois and Garrison equation coefficients	
c	sound speed	m/s
c_o	ray takeoff sound speed	m/s
c_w	UNESCO Sound speed equation coefficient	
D	UNESCO Sound speed equation coefficient	
f	frequency	Hz
f_1	boric acid relaxation frequency	Hz
f_2	magnesium relaxation frequency	Hz
f_c	carrier frequency	Hz
f_m	maximum Doppler shift	Hz
H	water column depth	m
h	channel impulse response	dB
$\hat{h}$	estimated channel impulse response	dB
I	intensity	watt/m^2
k	wavenumber	rad/m
L	Number of frames	frame
OVS	Over sampling rate	
p	sound pressure amplitude	Pa
P	complex sound pressure	Pa
P_1, P_2, P_3	Francois and Garrison equation coefficients	
R	symbol rate	symbol/sec
r	horizontal range	m
S	hydrophone sensitivity	dB
SPL	Sound pressure level	dB
t	time	sec
t_c	coherence time	sec
TL	transmission loss	dB
TVR	Transmitting voltage response	dB
VTX	Voltage at transmitter	V RMS
v	Lag	
$\vec{x}$	location	
z	vertical range	m
z_o	ray takeoff depth	m

Greek symbol	Description	Units
α	Attenuation	dB/m/kHz
ω	Angular frequency	rad/sec
ν	relative velocity	m/s
ρ_{xx}	auto-correlation	dimensionless
ρ_{xy}	cross-correlation	dimensionless
τ	time delay	sec
$\bar{\tau}$	mean time delay	sec
τ_{RMS}	root mean squared of time delay	sec
θ_0	ray takeoff angle	deg

Abbreviations	Description
ACF	Auto-Correlation Function
ADCP	Acoustic Doppler Current Profiler
B	Bretshneider
CCF	Cross-Correlation Function
CIR	Channel Impulse Response
CTD	Conductivity-Temperature-Density
DFO	Department of Fisheries and Oceans Canada
FD	Finite Difference
FE	Finite Element
FFP	Fast-Field Program
GPS	Global Positioning System
ISI	Inter-Symbol Interference
LFM	Linear Frequency Modulation
NOAA	National Oceanic and Atmospheric Administration
NM	Normal Mode
PDF	Probability Distribution Function
PE	Parabolic Equation
PM	Pierson-Moskowitz
PRN	Pseudo-Random Noise

RF	Radio Frequency
RMS	Root Mean Squared
SFC	Surface
SNR	Signal to Noise Ratio
SOFAR	Sound Fixing and Ranging
SPIRIT	Single Point Interface Roughness Inferring Transducer
SSP	Sound Speed Profile
TL	Transmission Loss
UNESCO	United Nation Educational, Scientific and Cultural Organization
UWAC	Underwater Acoustic Channel
VLA	Vertical Line Array
WAFO	Wave Analysis for Fatigue and Oceanography
WMO	World Meteorological Organization

Abstract

Underwater acoustic communication is a key enabler for civilian and military applications such as ocean sampling networks, offshore exploration, pollution monitoring and underwater surveillance (Akyildiz et al., 2005). Being able to understand and model the impact of time-varying environmental properties on the communication link could improve ray-tracing simulation fidelity which is currently one of the few tools available to test, analyze, and compare underwater communication schemes and performances. The DalComms1 sea trials took place in the summer of 2017 in an effort to better understand the impact of the environment on the underwater acoustic link performance, to test spread spectrum modulation techniques and to validate signal processing algorithms. The experiment was conducted on the Scotian Shelf and included transmissions of channel probing sequences, such as low frequency modulated and pseudo-random noise sequences, at ranges between one and ten kilometers. Other instruments such as an acoustic data current profiler, a conductivity-temperature-depth profiler, and a surface roughness measuring instrument complemented environmental data, including surface wind velocity, significant wave height and dominant wave period obtained from a nearby weather buoy and visual observations. The processing of the received signals allowed the extraction of important performance metrics such as estimated channel impulse responses, Doppler and delay spreads, as well as coherence times. Ray-tracing simulations through BELLHOP revealed an acceptable degree of agreement between the simulated deterministic result and the measurements. The behavior of the underwater acoustic channel was then investigated using a series of simulations with varying sound speed profiles, surface roughness, and relative motion between the source and receiver. The resulting means and variances were compared to the sea trial results and the series of simulations also allowed for the determination of the underwater acoustic channel's sensitivity to a variety of environmental perturbations. The result is a better understanding of the channel's variability and the importance of its contributors.

Acknowledgements

A project of this magnitude would not be possible without the support of people surrounding me. Thank you to my wife Kathryn who provided me with more support and love than I could have hoped for. I am also immensely grateful to Dr. David Barclay and Dr. Jean-Francois Bousquet for their guidance, patience and mentorship over the last two years.

This thesis would not have been possible without the DalComms1 sea trial and I would like to acknowledge the great work of UW-Stream lab, Dr. Paul Hines and Luna Ocean Consulting.

Finally, special thanks to Richard Cheel for the unconditional technical help provided.

Chapter 1

Introduction

1.1 Background

Underwater acoustic communication is a key enabler for civilian and military applications such as ocean sampling networks, offshore exploration, pollution monitoring, and underwater surveillance (Akyildiz et al., 2005). Despite having a clear advantage over radio and optical waves underwater, communication via the underwater acoustic channel (UWAC) represents significant challenges which are in part due to multipath propagation, attenuation due to absorption and spreading, and noise.

The variability in the channel's physical properties in both spatial and temporal domains at a multitude of length and time scales adds to the complexity. Changes in sound speed due to temperature, salinity, or pressure differences cause rays to refract, and changes in wind direction and intensity affect the surface roughness thereby affecting the path lengths. The result is a time-varying, fading channel accompanied with large delay spread and Doppler spread. Therefore, understanding how each physical property contributes to the variation in the channel impulse response (CIR) is important to improve underwater acoustic communication links.

The ability to account for time-varying properties accurately could improve the fidelity of ray-tracing simulation which is currently one of the few simulations available to test, analyze, and compare underwater communication schemes.

This thesis aims to identify the discrepancies and their respective sources between measured and simulated channel estimations to better understand and model the impact of time-variant channel properties on communication. The result is an increasing understanding of the channel's variability and the importance of its contributors.

1.2 Research objectives

The goal of this thesis is to quantify the impact of environmental physical properties on the characteristics of the UWAC. The outcome is a better understanding of the relation between the time-variance observed in underwater acoustic communication and its environment.

As such, the main objectives of this research are:

1. To complete the collection of physical channel characteristics such as the sound speed profile (SSP), sea surface roughness, current velocity profile, and bathymetry during DalComms1 sea trial for input of in-situ measurements into MATLAB simulations;

2. To extract channel estimation and communication performance from the recorded data;

3. To compare measured data and simulated ray trace data to identify the largest sources of discrepancy and uncertainty between the two;

4. To quantify the contributions of the main physical properties to the time-variance of the underwater acoustic channel.

1.3 Organization of the thesis

In chapter 1, the thesis was introduced and the objectives of the research are stated. In chapter 2, the main impairments to underwater acoustic communication and key concepts used during this research such as ray-tracing and channel estimation are introduced. In chapter 3, the field work procedure, instruments, and collected data are presented. In chapter 4, the methodology followed to extract information from the transmissions recorded during sea trials is explained and results are presented. Chapter 5 reviews the methodology followed during the simulation portion of the work, and presents results. Chapter 6 elaborates on the findings, makes comparisons between the measured and simulated data, and proposes explanations and conclusions. It is followed by a summary of the most important conclusions and closing remarks in chapter 7.

Chapter 2

Theory

Underwater acoustic communication has a variety of phenomenon and fundamental theories. This chapter explores those theories from the wave equation to channel estimation, while describing topics such as multipath propagation, transmission loss (TL) mechanisms, and ray-tracing theory.

2.1 Fundamentals of acoustic waves

Acoustic waves are longitudinal waves, meaning that they oscillate in the same direction they travel, similar to the waves created when a slinky is stretched and compressed along its longitudinal axis. Figure 2.1 illustrates such a scenario.

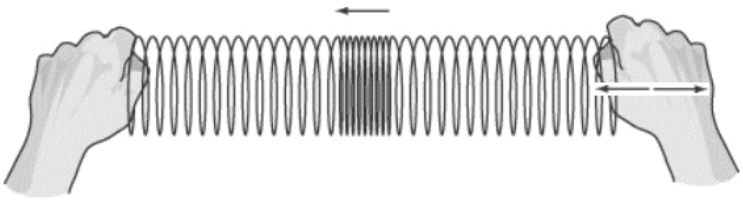

Figure 2.1: Longitudinal wave in a slinky adapted from Sparknotes (2011).

Acoustic waves are described by the wave equation which can be derived from the conservation of mass, conservation of momentum, and the state equations. Using those equations, one can derive the linearized wave equation (Feyman et al., 1969):

$$\nabla^2 p - \frac{1}{c}\frac{\partial^2 p}{\partial t^2} = 0, \tag{2.1}$$

where p is sound pressure, c is speed of sound, and t is time. Generally, the quantities p and c are functions of location, $\vec{x}$, and time.

The use of the linearized equation must satisfy a few assumptions: the medium is a Newtonian fluid with constant density in space and it is at rest. Also, the amplitude

of the pressure perturbations is small. Finally, there is no convection term (Campos, 1986).

The sound pressure, p, represents a wave with complex amplitude P. It is also the force applied per unit area and is normally expressed in Pa. This quantity is often expressed as a sound pressure level (SPL), a ratio, in the logarithmic space, between the sound pressure and a reference pressure, normally taken 1 m from the source for the case of a source level, or more generally taken to be 1 μPa underwater.

$$\text{SPL} = 20 \log_{10}\left(\frac{|p|}{p_0}\right) \text{ dB}. \tag{2.2}$$

The sound speed, c, is a function of temperature, salinity, and pressure. In seawater the sound speed ranges between 1450 m/s and 1650 m/s in deep water and exhibits a minimum, known as the Sound Fixing and Ranging (SOFAR) channel, at a depth of about 1 km (Jensen et al., 2000). The SSP shown in Figure 2.2 represents a generic open ocean SSP. Generally, the largest sound speed fluctuations occur near the surface boundary where the daily heating and cooling, precipitation, and the wind affect the mixed layer's temperature, salinity, and depth. In a shallow water environment, a large portion of the water column may be affected by the surface and bottom boundaries, increasing the complexity of the channel model.

A multitude of empirical equations have been derived to estimate the sound speed in seawater; United Nation Education, Scientific and Cultural Organization (UNESCO) equation, Mackenzie (Mackenzie, 1998), and Del Grosso's (Wong and Zhu, 1995) being three of the most popular. In this research, the equation used is the revised UNESCO equation (Wong and Zhu, 1995) due to Chen and Millero (Chen and Millero, 1977):

$$\text{C(S,T,P)} = C_w\text{(T,P)} + A\text{(T,P)}S^{3/2} + D\text{(T,P)}S^2, \tag{2.3}$$

where C_w, A, and D are constituted of 42 coefficients multiplied by expressions of temperature and water pressure. T is the water temperature in degree Celcius, P is the water pressure in bars and S is the water salinity in Practical Salinity Unit (PSU). The detailed equations and coefficients can be found in Appendix A.

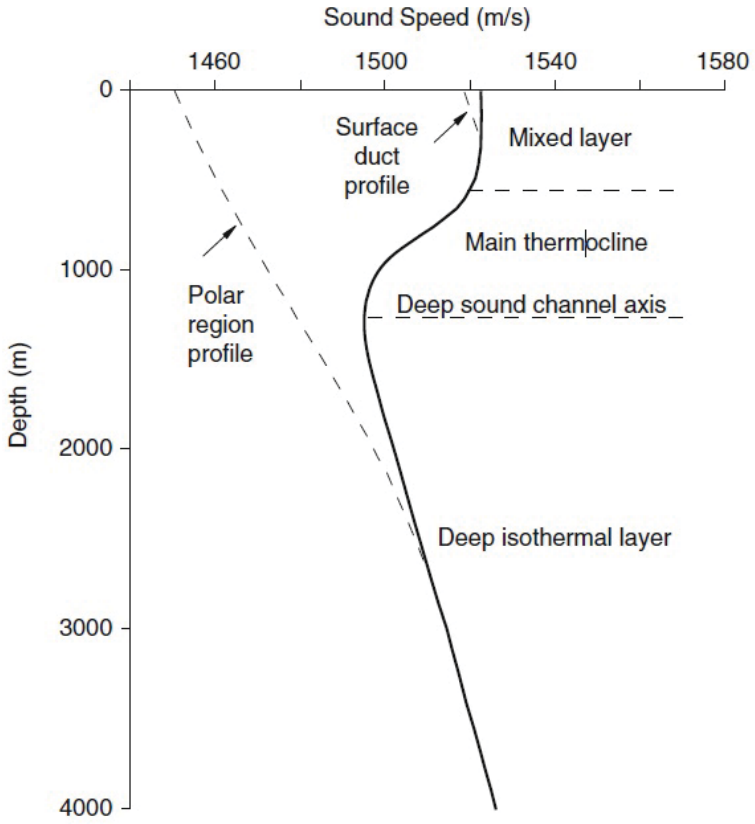

Figure 2.2: Generic soundspeed profile from Jensen et al. (2000).

2.2 Multipath propagation

Multipath refers to the propagation phenomenon that results from the many acoustic paths that connect the source and receiver in the underwater channel. In the UWAC, multipath is caused by the refraction of the wave due to the variable sound speed and reflection from the top and bottom boundaries. Because each path has a different length, the energy reaches the receiver at slightly different times, and therefore with different phases, causing interference.

Multipath is best represented by a simple ray-trace where the rays are perpendicular to the wavefront. Figure 2.3 illustrates the multipath propagation between a source and receiver with two reflected and two direct eigenrays (ray connecting the source and receiver). From the Figure 2.3, one can conclude that the location of the transmitter and receiver, the depth of the channel, and the SSP are the major parameters that determine the eigenrays and their arrival times.

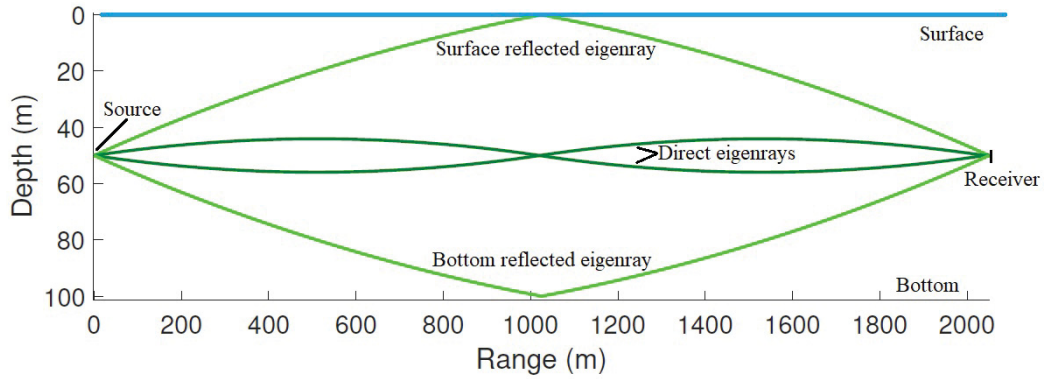

Figure 2.3: Example of multipath propagation with two direct and two reflected eigenrays.

Multipath is a significant problem in underwater acoustic communication because, combined with the slow speed of sound, it introduces long delay spreads possibly lasting over tens of symbols, or bits (Carbone and Hodgkiss, 2000). This could translates to hundreds of ms. When the channel is time-variant, the multipath also varies over time. Fading occurs when time-dependent multipath is present due to the constantly changing phase difference between eigenrays creating fluctuations in the resulting signal amplitude.

2.3 Transmission loss

The TL represents the reduction, expressed in dB, in acoustical intensity due to the wave traveling within the medium compared to a reference point placed 1 m away from the source. TL is mostly due to spreading and absorption but is also caused by scattering, reverberation, refraction, and dispersion (Akyildiz et al., 2005). This quantity is important because it is one of the most significant channel characteristics to determine communication reliability (Domingo, 2008).

The acoustical intensity is defined as the average rate of flow of energy through a unit area that is normal to the direction of propagation. Let I_0 be the intensity at 1 m from the source and $I(r, z)$ be the intensity at a point in the acoustic field. The TL can then be represented by:

$$\text{TL} = 10 \log_{10}\left(\frac{I(r,z)}{I_0}\right) \text{ (dB re 1 m)}. \tag{2.4}$$

For a plane wave in a homogeneous medium, the intensity is a function of pressure, medium density, and sound speed:

$$I = \frac{|p|^2}{\rho c}. \tag{2.5}$$

In this scenario, the TL can also be written as a function of sound pressure:

$$\mathrm{TL} = 20\ \log_{10}\left(\frac{p(r,z)}{p_0}\right)\ (\text{dB re 1 m}). \tag{2.6}$$

2.3.1 Geometric spreading

Geometric spreading refers to the geometric expansion of the wavefront. For a point source, the energy is evenly distributed over the surface area of the wavefront. This means that as the signal emitted by a point source propagates outwards, its intensity decreases proportionally to the surface area covered by its front. There are two common types of geometrical spreading: spherical, which is used to characterize a deep water column or a channel where its range is much greater than its depth, and cylindrical, which is used to characterize shallow water and account for the presence of the surface and bottom boundaries (Akyildiz et al., 2004).

When the spreading pattern is known (i.e. spherical or cylindrical) the ratio of acoustic intensity can be substituted by the ratio of the surface areas. For spherical and cylindrical spreading, the area covered by the wavefront is equal to $4\pi r^2$ and $2\pi rH$, respectively, where r is the radius from the source and H is the depth of the water column. By substituting these variables to eq. 2.4, the TL becomes:

$$\mathrm{TL}_{\text{spherical}} = 20\ \log_{10}(r) \tag{2.7}$$

$$\mathrm{TL}_{\text{cylindrical}} = 10\ \log_{10}(r), \tag{2.8}$$

where r is in meters. Note that TL incurred by geometric spreading does not depend on frequency.

2.3.2 Absorption

Absorption is a TL mechanism due primarily to viscosity and the relaxation of $\mathrm{B(OH)_3}$ and $\mathrm{MgSO_4}$ present in seawater and is therefore frequency dependent (Fisher and

Simmons, 1977). To a lesser extent, it is also a function of temperature and water pressure. One of the widely used models was proposed by Francois and Garrison (Jensen et al., 2000). This model takes into account three contributors: $B(OH)_3$, $MgSO_4$, and pure water, as shown in the following equation:

$$\alpha = A_1 P_1 \frac{f_1 f^2}{f_1^2 + f^2} + A_2 P_2 \frac{f_2 f^2}{f_2^2 + f^2} + A_3 P_3 f^2 \quad \text{dB/km}, \tag{2.9}$$

where α is the absorption as a function of frequency, f. The coefficients A_1 to A_3 and P_1 to P_3 represent the effects of water temperature and pressure respectively and f_1 and f_2 are the relaxation frequencies of boric acid and magnesium (Francois and Garrison, 1982).

Bellhop (Porter, 2011) is the propagation model used in this research and it uses a simplified absorption model known as Thorp's model (Thorp, 1967). This model does not account for water temperature nor pressure and defines absorption as follows:

$$\alpha = 1,0936\Big[\frac{0.1 f^2}{1 + f^2} + \frac{40 f^2}{4100 + f^2} + A_3 P_3 f^2\Big] \quad \text{dB/km}, \tag{2.10}$$

where f is in kHz. This model is considered valid below 50 kHz according to Thorp (1967), which is a smaller frequency range of validity compared to the Francois and Garrison model, however most underwater acoustic communication systems operate under 50 kHz and it is therefore well suited for simulations. Thorp's model was chosen to reduce the computation time of simulations compared to other models. Figure 2.4 shows the relation between the frequency and the absorption coefficient.

The absorption increases rapidly with frequency, especially above a few kHz, limiting the usable frequency band to below a few tens of kHz (Akyildiz et al., 2005).

Combining spreading and absorption while ignoring the effects of the boundaries or scattering within the medium, the overall TL in shallow water can be represented by the following expression:

$$\text{TL} = 10 \log_{10}(r) + \alpha r. \tag{2.11}$$

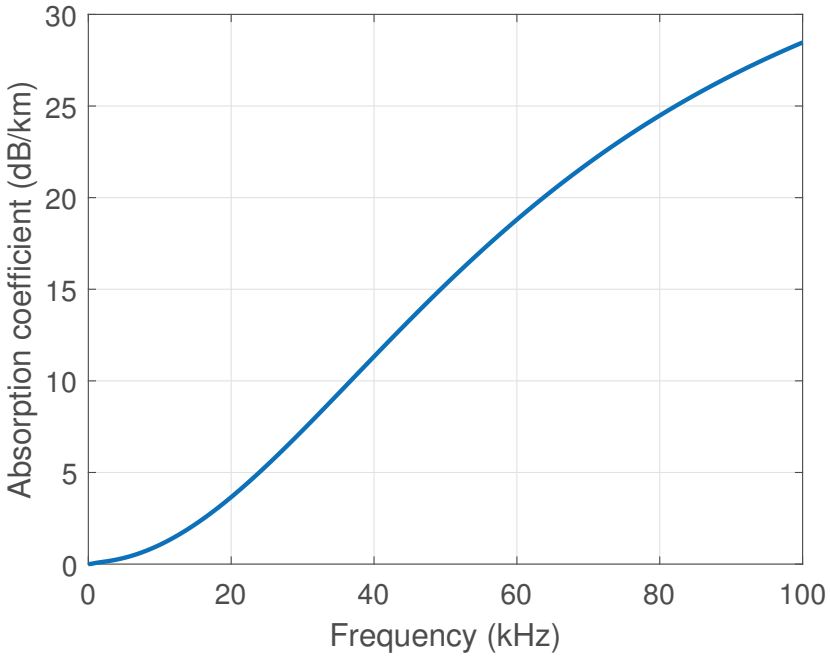

Figure 2.4: Thorp's absorption coefficient as a function of frequency.

2.4 Ray-Tracing

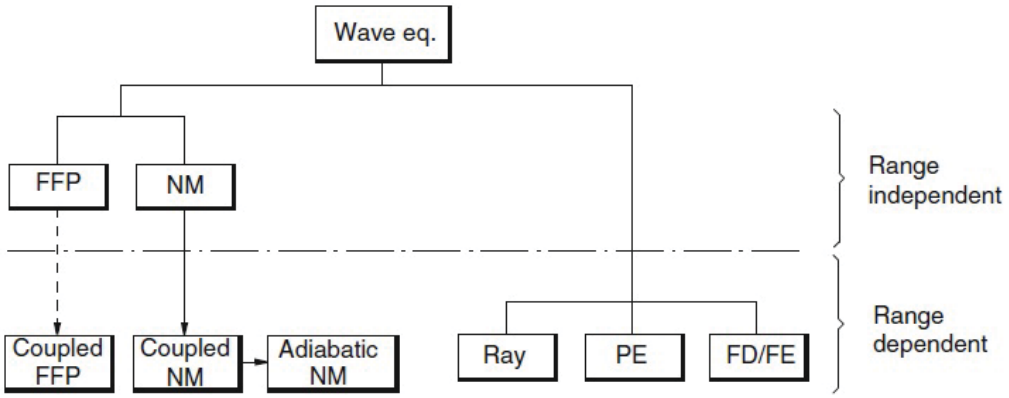

Figure 2.5: Underwater acoustic propagation model tree from Jensen et al. (2000).

Multiple options are available for underwater acoustic propagation models as shown in Figure 2.5. All models stem from the wave equation and fall under five categories: spectral or fast field program (FFP), normal mode (NM), ray-tracing, parabolic equation (PE), and finite difference (FD) or finite element (FE).

FFP and NM are integral form solutions to the wave equation and are therefore

normally used for low frequencies (i.e. below 5 kHz on a modern desktop computer) due to the increasing computation time with frequency and depth. While they are range independent, they can be extended to allow such dependence using various approximations. The PE, FD, and FE models are suited for range dependent and even 3 dimensional problems where the frequency is below 2 kHz. FD and FE are the most computationally intensive propagation models and are normally limited to short vertical and horizontal ranges. FD methods may be used to compute normal mode representations of the field.

Ray-tracing is advantageous at higher frequencies and when a visual representation of the ray-paths is required. Ray-tracing solves a set of ordinary differential equations (ODE) using initial conditions. Then, it steps forward in range solving the same set of ODEs using the previous results as initial conditions to determine the trajectory of the ray. This process solves one ray, while repeating the same steps as above for different launch angles solves an entire field. Since ray-tracing follows the rays during their travel, the travel time or delay can be calculated, which can be used in conjunction with ray amplitude to obtain a CIR.

Ray-tracing was chosen for this research because of the frequency of interest (around 2 kHz) and the range dependent nature of the measurement site.

2.4.1 Theory

In ray-tracing models, the trajectory of the rays is solved using Helmholtz's time independent form of the wave equation obtained through separation of variables (Jensen et al., 2000). Helmholtz's equation is the following partial differential equation:

$$\nabla^2 p + k^2 p = -\delta(\vec{x} - \vec{x}_s). \tag{2.12}$$

Supposing a solution of the form:

$$p(\vec{x}) = e^{i\omega t(\vec{x})} \sum_{j=0}^{\infty} \frac{A_j(\vec{x})}{(i\omega)^j} \tag{2.13}$$

yields the following first and second derivatives:

$$\frac{dp}{dx} = p_x = e^{i\omega t} \Big[i\omega t_x \sum_{j=0}^{\infty} \frac{A_j}{(i\omega)^j} + \sum_{j=0}^{\infty} \frac{A_{jx}}{(i\omega)^j} \Big], \tag{2.14}$$

$$\frac{d^2p}{dx^2} = p_{xx} = e^{i\omega t}\left\{ \left[-\omega^2 t_x^2 + i\omega t_{xx} \right] \sum_{j=0}^{\infty} \frac{A_j}{(i\omega)^j} + 2i\omega t_x \sum_{j=0}^{\infty} \frac{A_{jx}}{(i\omega)^j} + \sum_{j=0}^{\infty} \frac{A_{jxx}}{(i\omega)^j} \right\} \quad (2.15)$$

where the subscript x represent the partial derivative with respect to range.

Further reduction in complexity is achieved by separating this solution to the Helmholtz equation by orders of frequency (ω) and only keeping the highest order (ω^2). The remaining equations for $A_j(\vec{x})$ are known as the Transport equations (Jensen et al., 2000). This simplification is justified by the use of a high frequency approximation and leads to the Eikonal equation:

$$|\nabla\tau|^2 = 1/c^2, \quad (2.16)$$

where $\nabla\tau$ is the vector perpendicular to the wave fronts and c is the sound speed, leading to:

$$|\frac{d\vec{x}}{ds}|^2 = c^2|\nabla\tau|^2 = 1 \quad (2.17)$$

or

$$\frac{d\vec{x}}{ds} = c\nabla\tau, \quad (2.18)$$

where $\vec{x}(s)$ is the ray trajectory and s is the arc length along the ray.

Writing the 3-D Eikonal equation with the above substitution leads to the following equation:

$$\frac{d}{ds}\Big(\frac{1}{c}\frac{d\vec{x}}{ds}\Big) = \frac{-1}{c^2}\nabla c. \quad (2.19)$$

The following relationships can be derived for cylindrical coordinates:

$$\frac{dr}{ds} = c\ \xi(s) \qquad \frac{dz}{ds} = c\ \zeta(s) \quad (2.20)$$

and

$$\frac{\xi}{ds} = \frac{-1}{c^2}\frac{dc}{dr} \qquad \frac{\zeta}{ds} = \frac{1}{c^2}\frac{dc}{dz}, \quad (2.21)$$

where ξ and ζ are auxiliary variables used to solve $r(s)$ and $z(s)$. Solving this set of ODEs solves one step and using the solutions to fill in the subsequent step's initial

conditions solves the entire ray path. The first set of ODEs, at the source, is solved using the following initial conditions:

$$r = r_s \qquad z = z_s \qquad \xi = \frac{cos\theta}{c(0)} \qquad \zeta = \frac{sin\theta}{c(0)}, \tag{2.22}$$

where r_s and z_s are the range and depth of the source and θ is the launch angle.

This not only provides the trajectory, but also the phase of the ray through the time of travel.

To solve the pressure field, the following transport equation must be solved:

$$2\nabla\tau(\nabla A_0) + (\nabla^2\tau)A_0 = 0. \tag{2.23}$$

It can be shown that:

$$A_0(s) = A_0(0)\left|\begin{array}{cc} c(s) & J(0) \\ c(0) & J(s) \end{array}\right|^{1/2},$$

where $J(s)$ is the Jacobian under cylindrical coordinates with symmetry:

$$J = \left|\frac{d\vec{x}}{d(s,\theta,\phi)}\right| = r\left[\left(\frac{dz}{d\theta}\right)^2 + \left(\frac{dr}{d\theta}\right)^2\right] = \frac{r}{\sin(\theta_r)}\frac{dr}{d\theta}. \tag{2.24}$$

Assuming a point source with infinite homogeneous medium, the pressure field obtained is:

$$p(s) = \frac{1}{4\pi}\left|\begin{array}{cc} c(s) & \cos(\theta) \\ c(0) & -s^2\cos(\theta) \end{array}\right|^{1/2} e^{i\omega\int_0^s \frac{1}{c(s)}ds}.$$

Once all the rays that link the source and receiver, also known as eigenrays, are found and the pressure field is calculated, the TL may be computed in a few different ways. First, adding all of the eigenrays coherently accounts for the phase difference between them. The coherent summation simply sums the complex pressure, p, of all N eigenrays,

$$P^{(C)}(r,z) = \sum_{j=1}^{N} p(r,z). \tag{2.25}$$

Coherent TL is not the most realistic method as it usually introduces unrealistic interference patterns. Another way to combine the rays is to only sum the pressure amplitudes. Eq. 2.26 shows an incoherent TL calculation:

$$P^{(I)}(r,z) = \Big[\sum_{j=1}^{N} |p(r,z)|^2\Big]^{1/2}. \tag{2.26}$$

In this case, the phase is omitted by summing the square of the complex pressures.

Other methods such as semi-coherent TL are calculated the same way as incoherent TL with the addition of the contribution of the Lloyd-mirror interference pattern. Semi-coherent TL is often a favorable compromise between unrealistic hyper-details of coherent summation and the smoothed field of incoherent summation. Semi-coherent TL is defined as:

$$P^{(S)}(r,z) = \Big[\sum_{j=1}^{N} s(\theta_0)|p(r,z)|^2\Big]^{1/2}, \tag{2.27}$$

where $s(\theta_0)$ is shading function (Jensen et al., 2000),

$$s(\theta_0) = 2\sin^2\Big(\frac{\omega z_o \sin(\theta_0)}{c_0}\Big). \tag{2.28}$$

The shading function acts as a gain on the amplitude of the rays as a function of their take-off angle and depth, θ_0 and z_0, to represent interference patterns (Jensen et al., 2000).

Another parameter that has an impact on the ray-tracing output is the physical shape of the rays. The geometry of the rays' cross section is generally either geometric or Gaussian shaped (Porter and Bucker, 1987). In the geometric beam, the beam is shaped like an arrow head and the intensity decreases linearly away from the center. The more forgiving (in its implementation) Gaussian beam is shaped as a bell curve with 95% of the energy contained within two standard deviations of the mean. Those differ from the eigenray, which is a single line, to account for the energy between rays providing a more realistic result (Porter and Bucker, 1987).

2.4.2 Bellhop

Bellhop is one of the prominent ray-tracing codes and is written in Fortran and MATLAB by Porter (Porter, 2011). An overview of the Bellhop structure is shown in Figure 2.6.

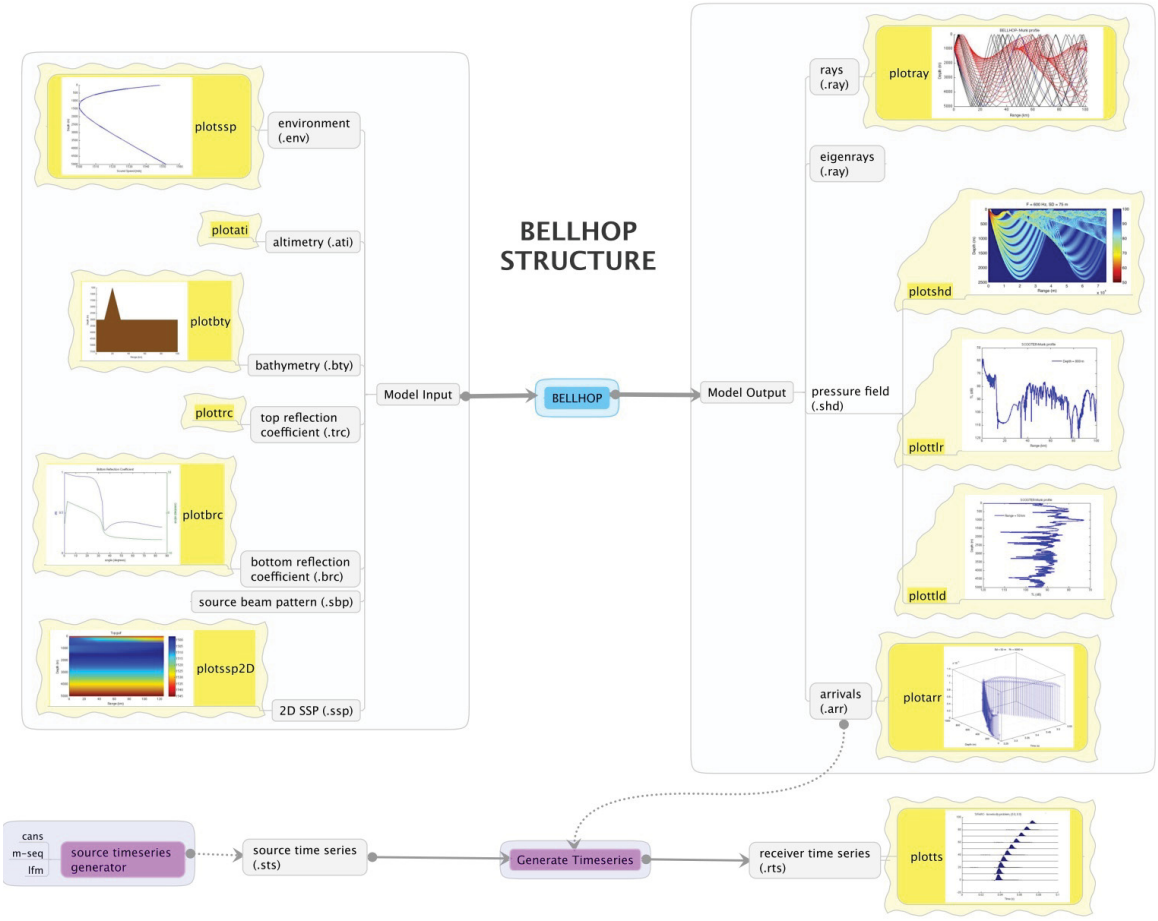

Figure 2.6: Structure of Bellhop from Porter (2011).

The inputs are an environment, a bathymetry, and an altimetry files. The environment file contains information such as the source and receivers' locations, the source frequency, the SSP and the properties of the boundaries. It also stores information about the run parameters such as step size and interpolation type. Some ray-tracing specific options such as geometric or Gaussian beam as well as the type of summation used to combine the rays are also available. The altimetry and bathymetry files are used to import a range dependent surface and bottom topography (Rodriguez, 2008).

The outputs are range and depth dependent TL, ray-trace, and amplitude-delay information which can be plotted using subroutines provided within the package.

2.5 Channel characterization

Channel estimation is a view into the state of the communication channel made possible by the transmission of a probing signal. In simple terms, it compares the original signal sent to the received signal to determine the impact of the channel on the sequence and therefore estimate channel characteristics such as TL, Doppler and delay spreads, as well as coherence time. This section describes the selection of a proper probing sequence and an example of channel estimation procedure.

2.5.1 Channel probing sequences

One of the most important design decisions to make when trying to estimate a CIR is to choose an adequate channel probing sequence. The probing sequence is used to emulate the transmission of impulses, which can't physically be transmitted, to measure how the response changes over time. In order to be an appropriate sequence, the reference signal must have a few properties such as a good auto-correlation function (ACF), defined in Eq. 2.29, and an appropriate duration. Two examples of such reference signals are the chirp, also known as Linear Frequency Modulated (LFM), and the pseudo-random noise (PRN) sequence. The ACF:

$$\rho_{xx}(t) = \int_{-\infty}^{\infty} x(t)x^*(t-\tau)dt \tag{2.29}$$

compares a time series to a lagged version of itself. A reference signal with a good ACF is a sequence that only displays a peak at lag 0 and has very low amplitude at all other lags. Such ACF is normally found in noise-like signals where each symbol is unrelated to the past and future symbols. Figure 2.7 shows a desirable ACF. This is important because the cross-correlation function (CCF) between the reference signal and the received signal depends on the ACF of the reference signal and the CIR:

$$\rho_{xy}(v) = \int_{-\infty}^{\infty} \rho_{xx}(v)h(\tau - v)d\tau, \tag{2.30}$$

where $h(\tau + v)$ is the CIR as a function of time delay and lag, τ and v, respectively.

Therefore, a poor ACF would induce CIR estimation errors due to, for example, the introduction of peaks in the CCF that are unrelated to the CIR.

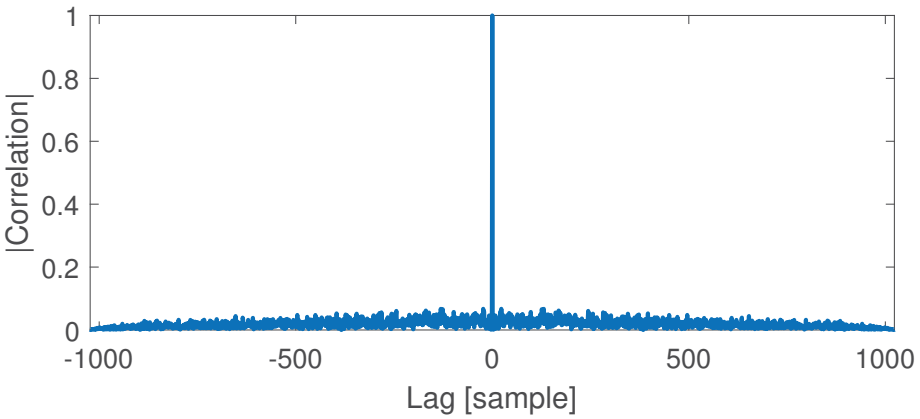

Figure 2.7: ACF of a 1024-bit long PRN sequence.

The duration of the sequence is also important because it dictates how much channel variation can be captured. The period of the sequence needs to be at least as long as the delay spread (time between the first and last resolved signal arrivals) in order to resolve the entire CIR, but its reciprocal must be as high as possible to track channel variability. Also, a long sequence becomes less favorable in operational applications since it can slow down communication rate and increase computational cost.

When using a PRN sequence, the two parameters affecting the duration of the sequence are the chips' period (T_c) and the total number of chips (K). A higher chip (pulse-shaped bit) count increases the length of the longest measurable path delay by reducing the PRN's side lobes by a factor of K (Novosel and Si, 2014) allowing separation of later taps (arrivals) from the noise. The chip period influences the resolution, or the smallest resolvable delay between two taps, since its ACF peak has a width equal to $2T_c$ (Rappaport, 1996).

Another way to access a sequence's ability to estimate a channel is to analyze its ambiguity function. Figure 2.8 illustrates the ambiguity function of the LFM and PRN sequences. The ambiguity function varies with respect to delay and Doppler shift and is defined as:

$$X(\tau, f) = \int_{-\infty}^{\infty} u(t)u^*(t-\tau)e^{2\pi i f t}dt, \tag{2.31}$$

where u is the signal, $*$ denotes complex conjugate, and f is the Doppler shift. In the absence of Doppler shift, the ambiguity function is simply the auto-correlation of the signal:

$$X(\tau) = \int_{-\infty}^{\infty} u(t)u^*(t-\tau)dt = \rho_{uu}(\tau). \tag{2.32}$$

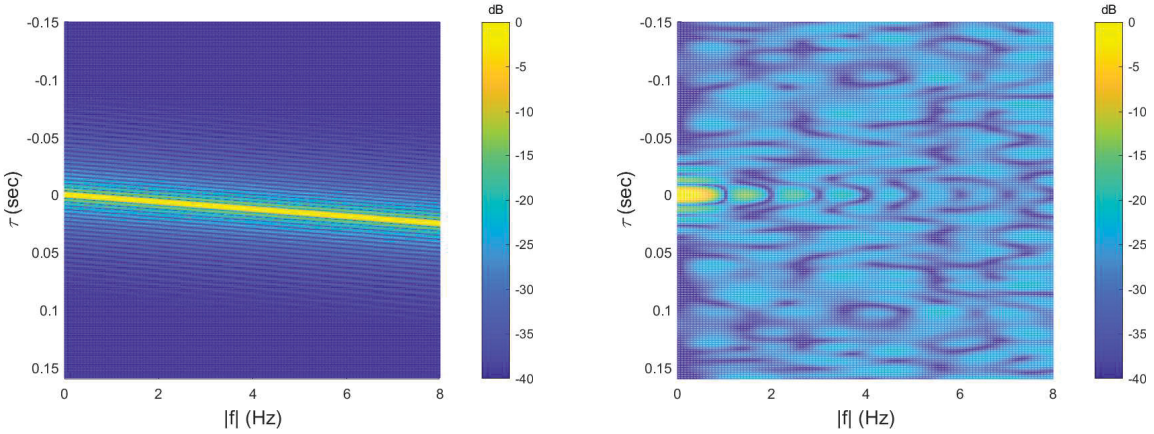

(a) A 320-Hz, 0.4-second LFM

(b) A 1024-bit PRN sequence.

Figure 2.8: Ambiguity functions for channel characterization.

The LFM displays strong properties against Doppler shift but its ambiguity function vanishes rapidly with time delay. Its immunity to Doppler shift (ambiguity function remains high across) comes at the expense of a delay shift of $\Delta\tau = f \times T/B$ which is referred to as delay-Doppler coupling. Also, the LFM has a poor delay resolution in time delay compared to other sequences (Walree, 2011).

The PRN sequence has a significantly different ambiguity function. The PRN shows a good resolution even at high time delays, but it does poorly in the presence of Doppler shift compared to the LFM. One of the consequences of its ability to cope with time delay is the added noise in the CIR since the ambiguity function does not vanish away from $\tau = 0$. In a rapidly fading environment, the CIR provided by the PRN sequence is expected to be noisier.

2.5.2 Channel estimation procedure

In its simplest form, channel estimation aims to provide an estimate of the channel impulse response, $\hat{h}(t,\tau)$, by comparing the received, $y(t)$, and original reference signal, $x(t)$. In general, to accomplish this, the reference signal must be up-sampled, pulse-shaped, and up-converted before being sent across the channel. Then, on the receiver's end, the signal is down-converted, down-sampled, and passed through a matched filter (cross-correlator) before a comparison with the reference sequence can be made. Figure 2.9 shows the diagram of such a procedure.

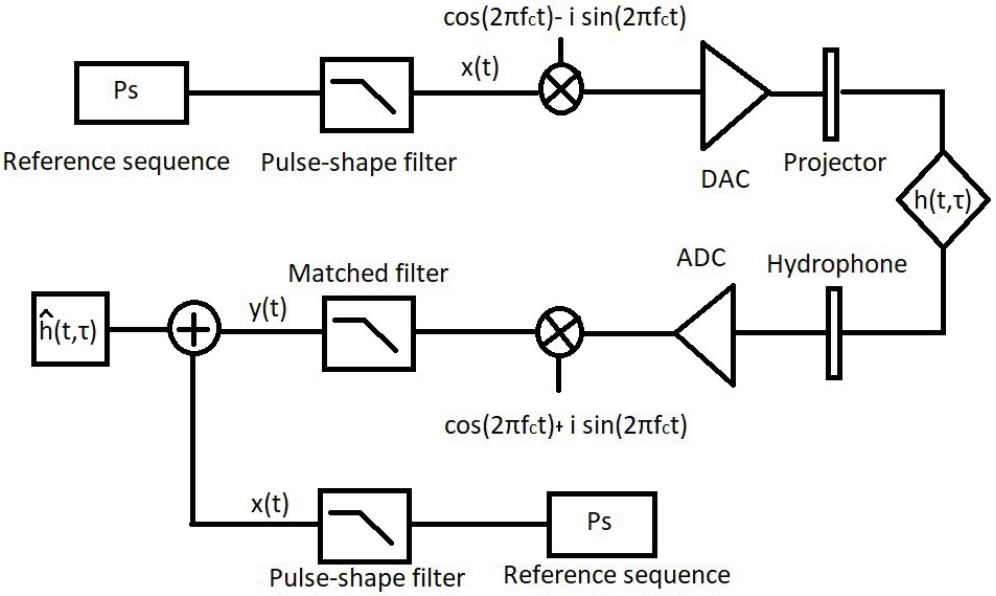

Figure 2.9: Block diagram of channel estimation procedure.

The comparison between $y(t)$ and $x(t)$ is done using the CCF between the two signals. The estimated CIR, $\hat{h}(t,\tau)$, is then expressed as:

$$\hat{h}(t,\tau) = (20\log_{10}(\|(\rho_{xy}(t,\tau)\|) + S) - (\text{TVR} + 20\log_{10}(\text{VTX})), \tag{2.33}$$

where ρ_{xy} is the normalized cross-correlation between the received and reference signal as a function of time, S is the hydrophone's sensitivity, TVR is the transmitting voltage response of the transmitter and VTX is the voltage at the transmitter.

Once the estimated CIR is obtained, it can be analyzed using multiple channel metrics to get a better understanding of the channel's properties and its impact

on communication. The amplitude fluctuations in the CIR, the root mean squared (RMS) delay spread, the Doppler spread, and the coherence time are a few examples of important figures.

The RMS delay spread gives insight into inter-symbol interference when analyzing a channel experiencing multipath. The RMS delay spread is defined as:

$$\tau_{\text{rms}} = \sqrt{\frac{\int_0^\infty (\tau - \bar{\tau})^2 h(\tau) d\tau}{\int_0^\infty h(\tau) d\tau}}, \tag{2.34}$$

where,

$$\bar{\tau} = \frac{\int_0^\infty \tau h(\tau) d\tau}{\int_0^\infty h(\tau) d\tau}. \tag{2.35}$$

The delay spread describes the dispersive nature of the channel but does not provide any information about the time variations caused by the relative motion between the source and receiver. In that case, the Doppler spread and coherence time are more appropriate parameters.

The Doppler spread is the spectral broadening of a signal and describes the range of frequency for which the Doppler shift is non-zero. The impact of the motion between the source and receiver is deemed unimportant when the Doppler spread is much smaller than the baseband signal bandwidth (Kilfoyle and Baggeroer, 2000). Low Doppler spread channel can also be seen as a slow fading channel. The maximum Doppler shift, f_m, is defined as:

$$f_m = \frac{v f_c}{c}, \tag{2.36}$$

where v is the relative velocity between the source and receiver, c is the sound speed in the medium and f_c is the carrier frequency. The Doppler spread is the difference between the maximum Doppler shift on both sides of the carrier frequency. The RMS delay spread represents the variance of the spread and is normally a more meaningful figure.

On the other hand, coherence time is the duration of time over which an impulse response is deemed invariant, showing how similar the channel's amplitude is from one time to the next. Therefore, the coherence time is inversely proportional to the Doppler spread. In general, the coherence time is defined as the time over which the

correlation function, ρ_{yy}, is above 0.5, or half the maximum amplitude. In this case, the coherence time is approximately given by (Rappaport, 1996):

$$t_{coh} \approx \frac{9}{16\pi f_m}, \tag{2.37}$$

where f_m is the maximum Doppler shift.

For example, two signals arriving at an interval greater than the coherence time are expected to be affected differently by the channel. This means that a coherence time smaller than the reciprocal of the bandwidth implies that the channel will change during the transmission of the message, thus causing distortion at the receiver.

2.6 Related work

This section places the research in context by describing a few recent experiments and their contribution to the field of underwater acoustic communication.

Recent work has laid the foundation to better understand the impact of different contributors on the received signal and to characterize them statistically.

One way to increase our understanding about the behavior of the UWAC is to compare measurements, such as the estimated channel impulse response, of a well defined underwater communication experiment to simulations with similar environmental parameters. The comparison between simulated and measured channel impulse response usually starts with an experiment at sea which including the transmission and reception of a channel probing sequence. Most experiments also include the recording of environmental data such as bathymetry and bottom properties, SSPs, current velocity, dominant surface waves height and winds as a function of time and space to determine causality between the environment and the received signal's characteristics.

Then, most studies analyze the channel impulse response via metrics such as TL, Doppler and delay spreads, coherence time and bandwidth as part of a temporal and/or spatial analysis. This analysis answers the question: how much is the signal transformed during its travel across the medium?

In the last two decades, shallow water experiments such as KauaiEx (Song et al., 2008), AUVFest07 (Yang, 2013), RACE08 (Qarabaqi and Stojanovic, 2009) and SubNet 2009 (Tomasi et al., 2010) provided insight into the relationship between the varying conditions and their impact on underwater acoustic communication. Some

important take-aways from these experiments are that the surface roughness greatly reduces the temporal coherence of a given multipath due to both signal fading and rapidly varying phase (Yang, 2013). In rough sea, temporal coherence of less than 200 ms has been observed for a high frequency signal in a 5 km long channel and during a very shallow water experiment, an increased delay spread and a diminished coherence time were linked to an increase in surface roughness driven by the wind (Badiey et al., 2000). It was also shown that an open ocean UWAC exhibits lower coherence time compared to one located in a protected bay (Yang, 2013). Other factors impacting the coherence time have also been identified, such as water temperature fluctuations which can greatly reduce the temporal coherence of the rays traveling through them (Carbone and Hodgkiss, 2000). With respect to the fluctuations in amplitude, while some studies found that Rayleigh fading matches their measurements, others have observed that Rician or log-normal were a better fit.

After the data is collected and analyzed, some studies go one step further and attempt to model the impairment inflicted on the signal by those environmental variations. For example, Qarabaqi and Stojanovic (2009) modeled the time-invariant response of a wideband acoustic channel as a superposition of multiple propagation paths where all paths are approximated by a filter of identical shape but different gain. The time-varying portion of the response is modeled by multiplying a random gain to each path. The gain is determined by a time-varying local average and an additional, more rapidly varying, random component in each path gain. The latter represents fast fading which is caused by channel variations within a window of stationarity and is found to be well-matched with a Rayleigh distribution leading to an overall Rician fading on each path. Radosevic et al. (2009) also reached the conclusion that the channel fading was Rician distributed when analyzing the data from KauaiEx, contributing to the answer to the question: what is transforming the signal?

Yang (2013) investigated the change in amplitude as a function of time by using a mean-to-standard deviation ratio and showed that rough sea paths are less deterministic. He also showed that despite the randomness, the deterministic contribution is too strong to assume a Rayleigh distribution. Also, Yang noted that the distribution change depends not only on the environment, but also on different paths within an environment.

This thesis expands on previous work by providing analysis on a new shallow water UWAC experiment complemented by a rich environmental data set. The investigation of the impact of different physical properties of the channel on performance is also in-line with recent studies, but the use of ray-trace simulation ensembles to quantify contributions has not been done in the context of underwater acoustic communication with the exception of Hamm et al. (2015) which used Monte Carlo Bellhop simulations to look at TL and bit error rate in an Arctic environment.

Chapter 3

Field Work

In this chapter the deployment location and procedure, as well as the data collection process are described. The data used in this thesis were collected during the DalComms1 sea trial ran by the Department of Electrical and Computer Engineering of Dalhousie University. The overarching goal of this series of experiments was to develop better underwater communication schemes. To this end, the objectives were the following:

1. To extract the propagation properties using a channel interrogation sequence;
2. To test spread spectrum modulations for reliable underwater acoustic link; and
3. To test timing recovery/Doppler compensation algorithms.

The scope of this research falls within the first objective and focuses on the analysis of one of two channel interrogation sequences transmitted during the experiment. The results from the other objectives will not be presented nor discussed in this thesis.

3.1 Site description

Chosen for its proximity, the Scotian shelf offers a relatively mild shallow-water underwater acoustic communication environment. Figure 3.1 shows the location of the receiver and the different stations where the source was deployed. The site was 10 km away from land south of Prospect, Nova Scotia and the propagation path ran parallel to the shoreline. This location was chosen for its depth and relatively flat bathymetry. The bottom is characterized as sand with over 50% gravel translating to a sound speed of about 1800 m/s and a density neighboring 2 g/cm^3 (Hamilton, 1970). The bathymetry of the UWAC is shown in Figure 3.2.

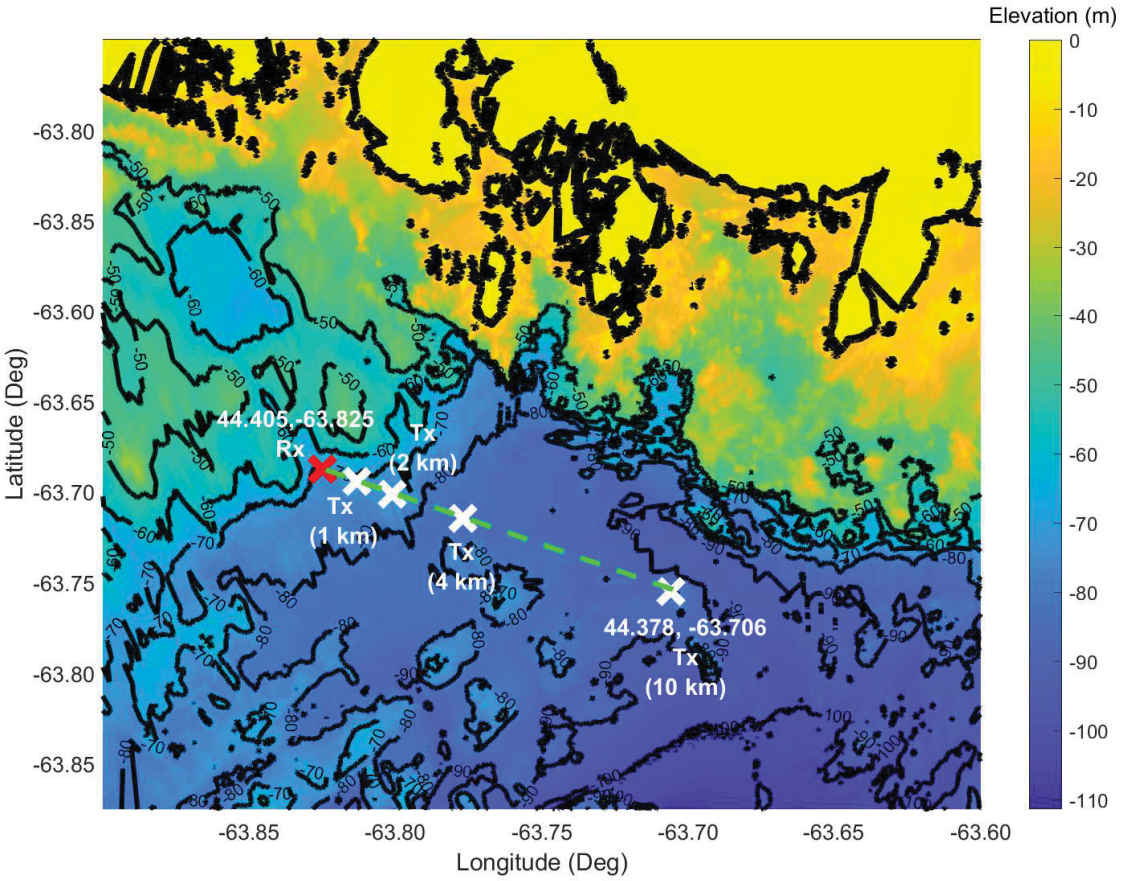

Figure 3.1: Bathymetry around the sea trial area with approximate source and receiver stations with 10 m contour lines.

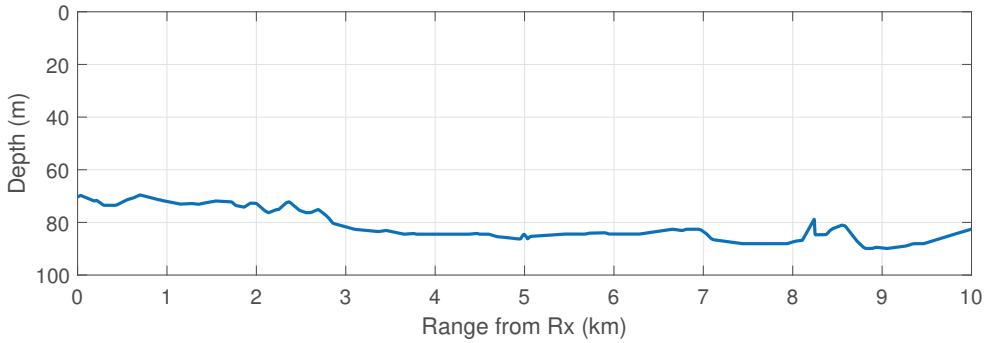

Figure 3.2: Bathymetry from the receiver to furthest source location.

The bathymetry of the study area and bottom composition were provided by the Canadian Hydrographic Services at the Department of Fisheries and Oceans Canada (DFO) and the data were manipulated to obtain a polar map with a resolution of

1 m (interpolated from the original 10 m resolution), shown in Figure 3.3. Once centered on the receiver's location (fixed during the experiment), this bathymetry format allows easy importation into Bellhop by simply choosing a bearing along which the propagation modeling is to be computed.

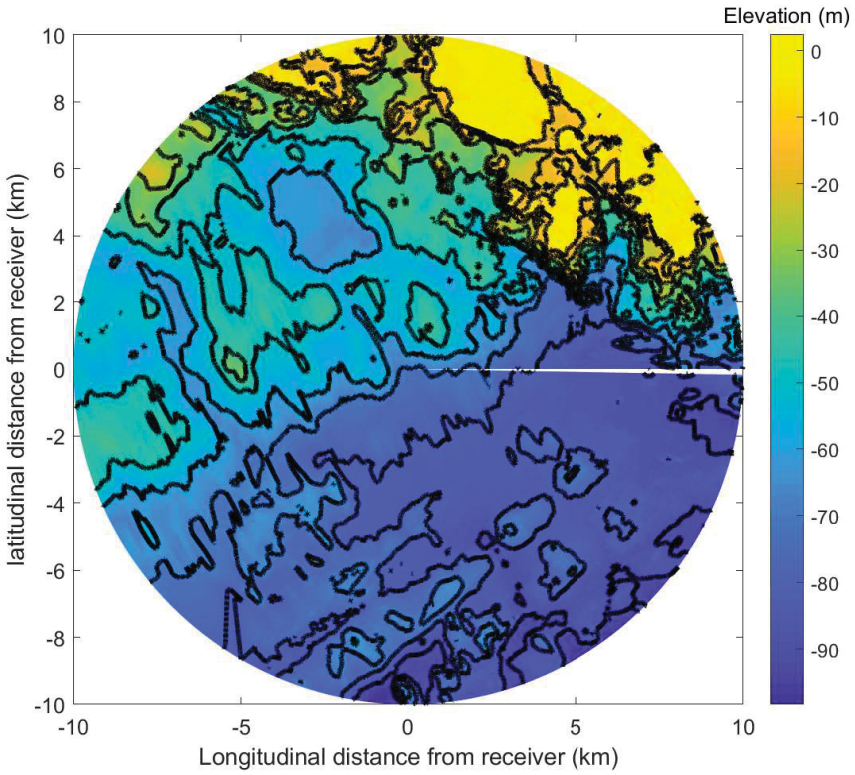

Figure 3.3: Bathymetry centered on receiver position (44.405N, 63.825W) in polar coordinates with depth in meters.

The experiment took place on July 26-28 2017 and during that time period, the wind direction was mostly southwesterly with a mean speed of about 6 m/s and the sea state varied between sea state 2 and sea state 3 on the World Meteorological Organization (WMO) sea state scale according to wind speeds and visual observations. The air temperature varied between 14^{o}C and 17^{o}C and the water surface temperature was approximately 16^{o}C.

The National Data Buoy Center website sponsored by the National Oceanographic and Atmospheric Administration (NOAA) provides historical records of meteorological data on an hourly basis at specific buoys. Buoy #44258 is installed at the mouth of the Halifax Harbour, approximately 30 km from the deployment site. The data

recorded during the experiments is reported in Table 3.1 where WDIR, WSPD and GST are the wind direction, speed and gust speed respectively. WVHT and DPD are the significant wave height and dominant wave period, and, PRES, ATMP and WTMP are the atmospheric pressure, air and water temperatures near the surface.

Table 3.1: Data recorded at buoy #44258 (44.500N 63.4W) during the experiments.

DATE (yr-mo-day)	TIME hh:mm	WDIR [deg]	WSPD [m/s]	GST [m/s]	WVHT [m]	DPD [sec]	PRES [mb]	ATMP [^{o} C]	WTMP [^{o} C]
2017-07-28	18:00	190	4.0	5.0	0.7	4	1009.8	16.6	15.8
2017-07-28	17:00	200	5.0	6.0	0.7	4	1010.0	16.5	15.7
2017-07-28	16:00	200	7.0	8.0	0.7	8	1010.0	16.5	15.7
2017-07-28	15:00	200	6.0	8.0	0.6	4	1010.2	16.3	15.6
2017-07-28	14:00	200	6.0	6.0	0.6	8	1010.3	16.3	15.6
2017-07-28	13:00	210	6.0	7.0	0.7	4	1010.3	16.0	15.6
2017-07-28	12:00	210	6.0	8.0	0.7	4	1010.6	15.9	15.6
2017-07-28	11:00	200	6.0	8.0	0.7	4	1010.4	15.7	15.6
2017-07-28	10:00	220	6.0	7.0	0.7	4	1010.8	15.4	15.7
2017-07-28	09:00	220	6.0	7.0	0.7	7	1010.8	16.1	15.8
2017-07-28	08:00	210	6.0	7.0	0.7	7	1011.1	16.1	15.9
2017-07-27	18:00	210	6.0	7.0	0.8	7	1016.1	16.0	16.1
2017-07-27	17:00	200	6.0	7.0	0.8	7	1016.6	16.1	16.4
2017-07-27	16:00	210	6.0	7.0	0.8	7	1017.1	16.2	16.6
2017-07-27	15:00	210	6.0	7.0	0.7	7	1018.0	16.1	16.5
2017-07-27	14:00	210	6.0	7.0	0.6	7	1018.0	16.1	16.4
2017-07-27	13:00	200	6.0	6.0	0.7	7	1018.3	16.1	16.4
2017-07-27	12:00	210	5.0	6.0	0.7	7	1018.8	16.4	16.2
2017-07-27	11:00	210	4.0	5.0	0.6	7	1018.9	16.3	16.2
2017-07-27	10:00	220	4.0	4.0	0.8	7	1018.8	16.1	16.2
2017-07-27	09:00	220	3.0	3.0	0.7	7	1018.7	16.0	16.2
2017-07-27	08:00	220	2.0	3.0	0.8	7	1018.6	15.9	16.3
2017-07-26	17:00	170	3.0	3.0	1.1	7	1021.7	17.0	17.5
2017-07-26	16:00	130	3.0	3.0	1.2	8	1021.9	17.1	17.6
2017-07-26	15:00	40	1.0	2.0	1.4	7	1022.0	17.0	17.2
2017-07-26	14:00	40	2.0	3.0	1.3	8	1022.1	16.5	16.3
2017-07-26	13:00	0	4.0	4.0	1.3	7	1022.3	16.0	15.9
2017-07-26	12:00	0	4.0	5.0	1.2	8	1022.1	14.6	15.7
2017-07-26	11:00	360	6.0	7.0	1.6	8	1022.0	13.9	15.6
2017-07-26	10:00	360	6.0	7.0	1.4	7	1021.7	14.1	15.5
2017-07-26	09:00	330	4.0	5.0	1.6	8	1021.2	14.4	15.0
2017-07-26	08:00	350	5.0	6.0	1.6	8	1020.7	14.5	15.1

3.2 Deployment procedure and data collection

The data collection took place between July 26^{th} and July 28^{th} 2017 during the DalComms1 sea trial and all operations were completed between 08:00 ADT and 18:00 ADT. The motor vessel used was the *Saorsa*, a 40 ft long and 12 ft wide Northumberland hull Cape Islander. As depicted in Figure 3.4, an acoustic Doppler current profiler (ADCP) and a Single Point Interface Roughness Infering Transducer (SPIRIT) were mounted on the port side aft and forward respectively. The starboard side was reserved for the deployment of overboard equipment such as the 5-element vertical line array (VLA) and the transmitter. While on station, Conductivity-Temperature-Density (CTD) profiler casts were also done on the starboard side with the help of a pulley.

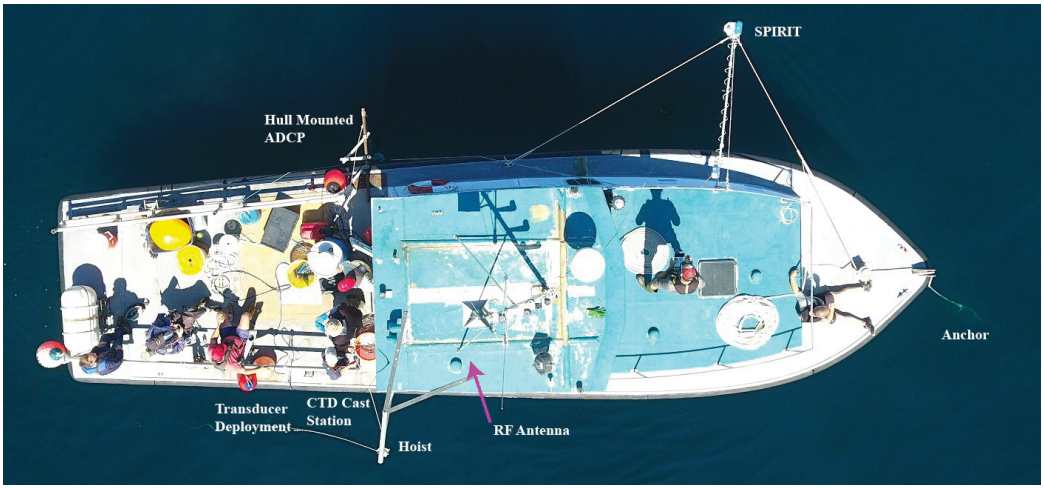

Figure 3.4: Top view of the Saorsa during deployment.

During the sea trial two types of measurements were completed. First, the UWAC was studied using a CTD, ADCP and SPIRIT. Second, multiple channel estimation training sequences were sent and received at ranges of $0.5, 1, 2, 4, 8$, and 10 km. Transmissions were sent at two different depths, within and below the thermocline, at most transmission locations.

A depiction of the deployment is shown in Figure 3.5. The main receiver, a 5-element VLA, was deployed mid-depth (38 m) without any surface expression to limit its interaction with the surface layer. A 60-kg anchor and two buoyancy floats were also used to reduce motion at the receiver. The acoustic data and power source were

stored on hard drives located in the TR-ORCA pressure case. Despite the deployment of a secondary receiver connected to a RF (radio frequency) float, the asset was not used due to water ingress rendering the float unusable. The transmitter was deployed overboard and transmissions were made at two depths: within the thermocline and at the same depth as the receiver. The transmitter was pulled down by a weight to reduce its motion.

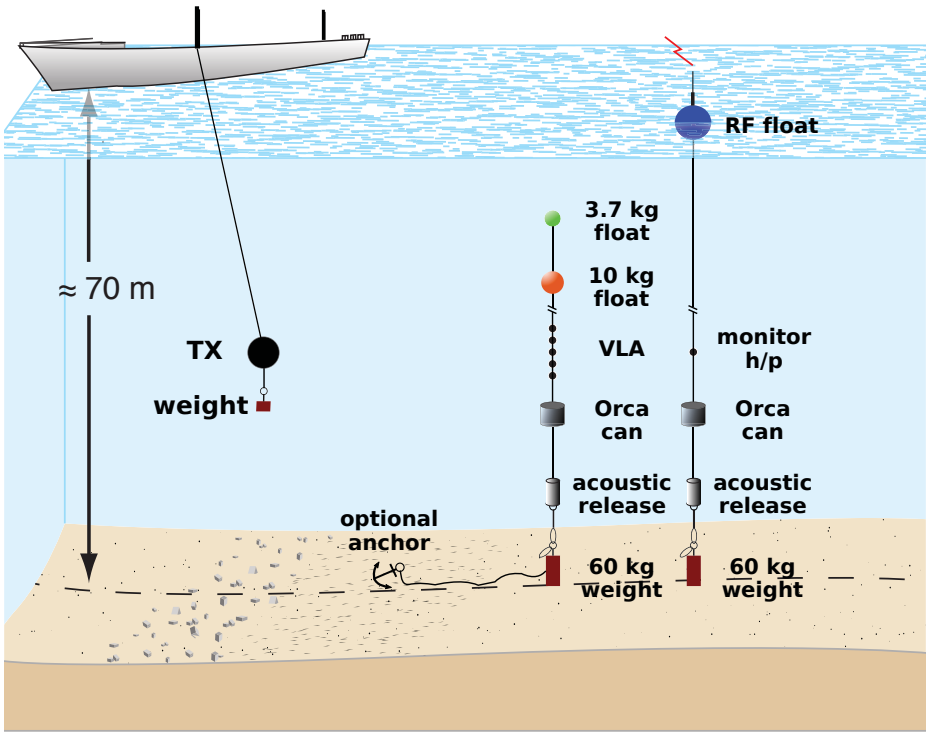

Figure 3.5: Cross-section of the sea trial deployment.

A total of 7 wavefiles with durations between 6.5 and 10 mins were transmitted at every station. The wavefile of interest in this research was a 9 min long 1024-bit PRN (Gold code) channel probing sequence. The transmission schedule of the PRN sequence is shown in Table 3.2 and the exact distance between the source and receiver is depicted in Figure 3.6.

Table 3.2: GPS position and time of transmission.

VLA mooring	N $44^o24.166'$, W $63^o49.257'$	day 1 & 2
VLA mooring	N $44^o24.174'$, W $63^o49.284'$	day 3
Transmitter @ 1 km (short sequence)	N $44^o24.144'$, W $63^o48.522'$	day 1 - 12:48
Transmitter @ 2 km	N $44^o24.083'$, W $63^o47.893'$	day 3 - 15:10
Transmitter @ 4 km (day 2)	N $44^o23.615'$, W $63^o46.338'$	day 2 - 14:00
Transmitter @ 4 km (day 3)	N $44^o23.503'$, W $63^o46.401'$	day 3 - 11:35
Transmitter @ 8 km	N $44^o23.520'$, W $63^o43.666'$	day 1 - 16:24
Transmitter @ 10 km	N $44^o23.315'$, W $63^o42.089'$	day 2 - 11:02

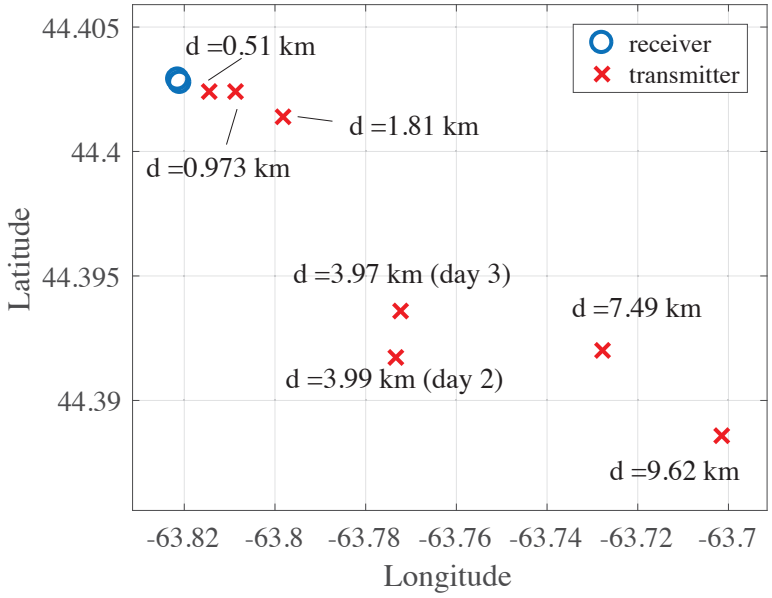

Figure 3.6: Recorded position of the equipment.

While on station, CTD casts and ADCP recording were completed as often as possible while SPIRIT was running all day. Visual estimation of wave direction was also recorded.

3.2.1 Oceanographic Instruments

This section describes the instruments used in greater detail and presents the data collected by each of these devices. It is divided into three parts: CTD, ADCP and SPIRIT.

CTD

A CTD profiler records the conductivity, temperature, and pressure while traveling through the water column. It also records time and GPS location at the surface at the beginning and the end of the cast. This data provided speed of sound as a function of depth at a specific location and time.

Figure 3.7: Hand-held Sontek Castaway CTD profiler.

During DalComms1, the hand-held Sontek Castaway CTD was used to collect data. Over the span of 3 days, 70 CTD casts were completed. Among these casts, four were done near the receiver's location. All other casts were made at the transmitting stations and all cast locations are shown in Figure 3.8. Most of the CTD casts were completed concurrently with data transmission which explains the highly concentrated cast areas. The gaps in CTD casts are due to movement between stations and other critical operations such as deployment and recovery of various equipment. The highest cast count at a given station happened at the 4 km station on day 3 where 20 casts were completed in 100 minutes.

Figure 3.9 shows SSPs from CTD casts near the receiver's location during the 3-day period. While the SSP remained fairly constant over the span of each individual day, they are noticeable differences between days. On day 3, the mixed layer near the surface was more apparent and went down to 23 m, or about 5 m deeper than that

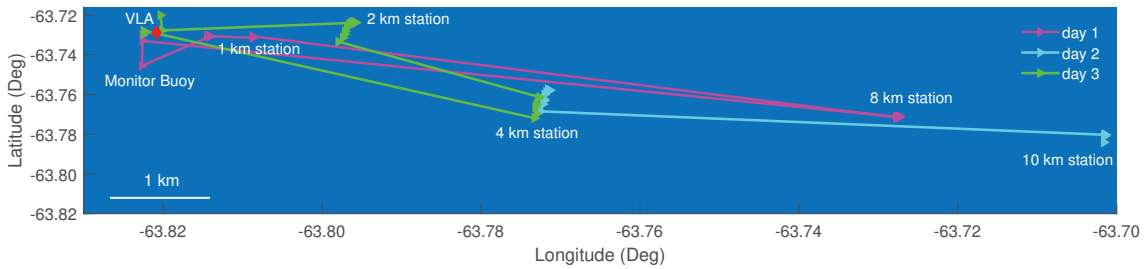

Figure 3.8: CTD cast locations.

of day 1. The mixed layer is followed by a shallow thermocline extending to 25 m on the first day and 35 m on the third day. Below that, the temperature stabilized around 4.5^{o}C. The salinity was slightly higher on the first day and the difference was the greatest between 20 and 30 m. This translated to similar sound speeds at the top and bottom of the water column for both days with a difference of up to 15 m/s between 20 and 25 m.

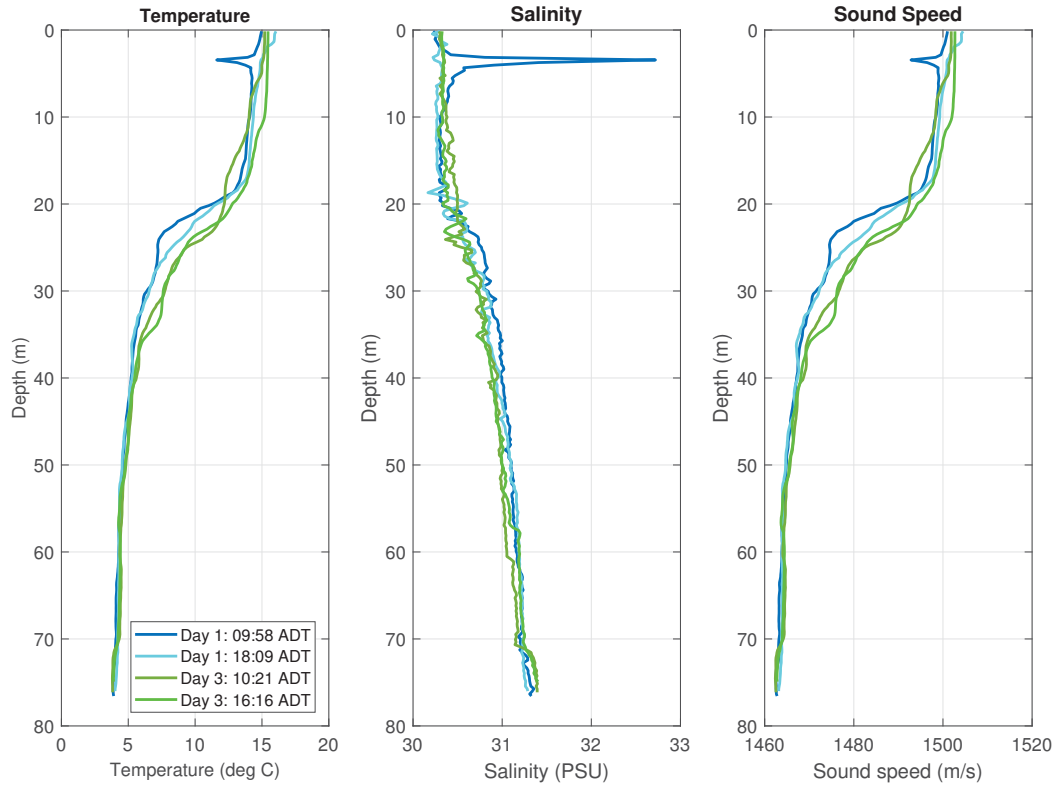

Figure 3.9: Temperature, salinity and SSPs taken near the receiver.

From Figure 3.9, the SSP at the receiver location was fairly steady with small variations in the mixed layer depth. At a depth of 40 m, the receiver was below most of the variation and the local sound speed remained approximately constant during the entire experiment. The expected result is a downward refracting environment inhibiting surface interactions. The temperature and salinity anomaly seen on the first SSP at 4 m deep was interpreted as a sensor error and has replaced by the interpolation between the preceding and succeeding sample.

Figure 3.10 superposes all the SSPs taken during the experiment. The conclusions are similar to the profiles taken at the receiver, where the mixed layer and bottom half of the water column sound speeds vary little while greater variance is observed between 20 m and 35 m. The source and receiver remain under the thermocline favoring bottom interactions.

To verify the impact of the thermocline on communication, a few transmissions were completed with the projector at a depth of 26 m, placing the source within the area experiencing the strongest vertical sound speed gradient.

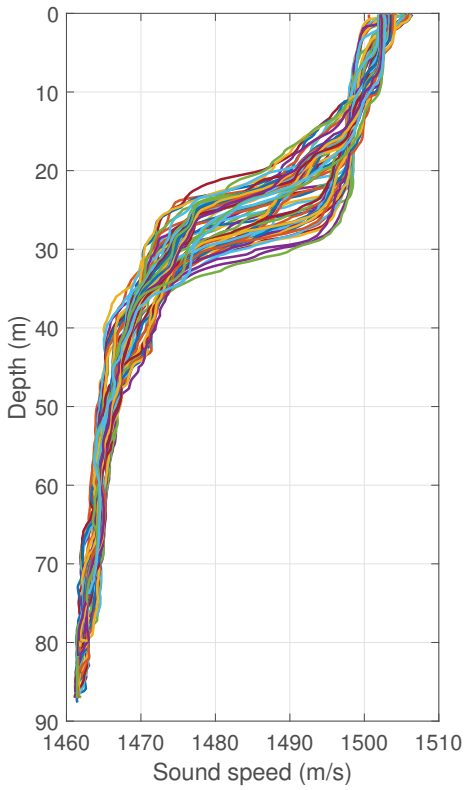

Figure 3.10: 70 SSPs taken between 26-28 July 2017.

Figure 3.11 shows the sound speed anomalies, relative to the mean, of those 70 profiles as a function of time. On day 1, our longest day on site, the impact of daily heating is clearly visible. Over the span of the day, the mixed layer deepens from 20 m to 30 m explaining the variance seen in Figure 3.10. Day 2 and day 3 were very constant, but the variability of mixed layer depth over short (minute) time scales can be as much as a few meters.

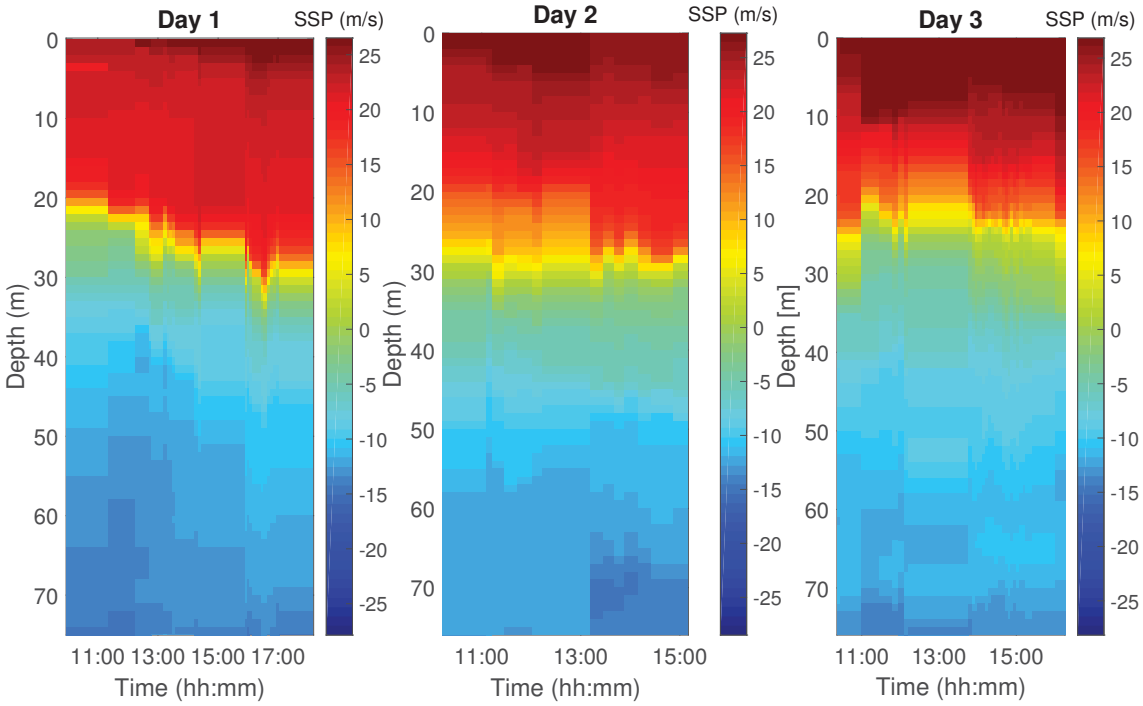

Figure 3.11: Sound speed anomalies as a function of time for each day.

ADCP

The ADCP used was the Teledyne Marine Workhorse with bottom tracking enabled. The instrument was downward facing and mounted to the ship via a custom mount. Its operation was limited to on-station use due to mount limitations prohibiting data collection while moving.

The ADCP data provides current velocity profiles as a function of time. Figure 3.12 shows the time-averaged horizontal flow velocity as a function of depth for a recording taking on day 3.

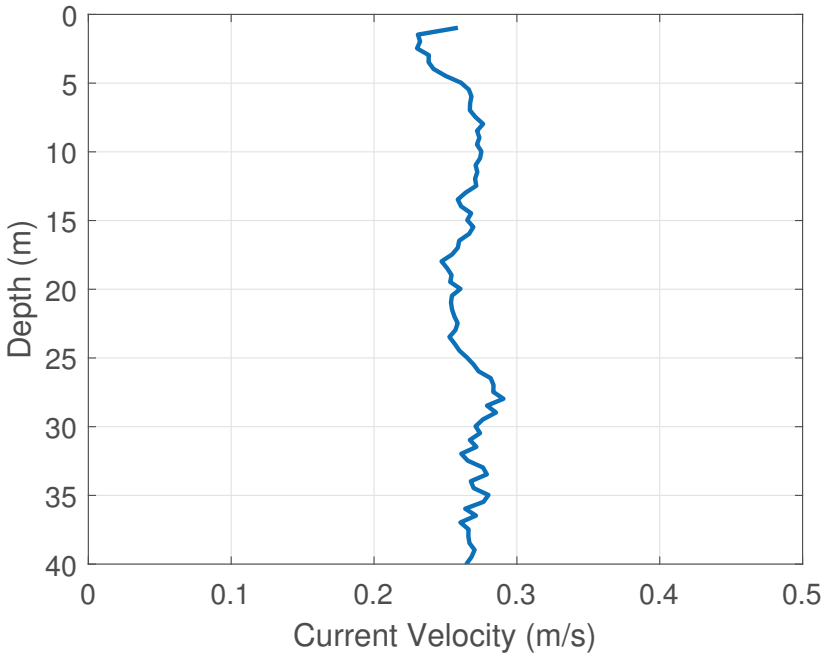

Figure 3.12: Time-averaged current velocity as a function of depth on day 3.

Figure 3.12 shows only the flow in the first 40 m of the channel due to the sensor's range. The recording was 120 min long and during that time period the current speed as a function of depth is fairly constant, only varying by a few cm/s. With respect to ADCP, the most important data for our analysis were the current at the source and receiver's depth because it provides information about the motion they are subject to. During this recording, the average horizontal velocity at the source depth was 26 cm/s.

Figure 3.13 provides information about the direction of the flow. The mean direction of the current is approximately 120^o off the source-receiver axis but varies greatly with time. Visual observations taken during the recording reported a general surface wind direction 85^o off of the channel axis. The 35^o difference between the two measurements may be attributed to the Ekman layer, thus the visual and instrumental measurements of the flow direction are in agreement.

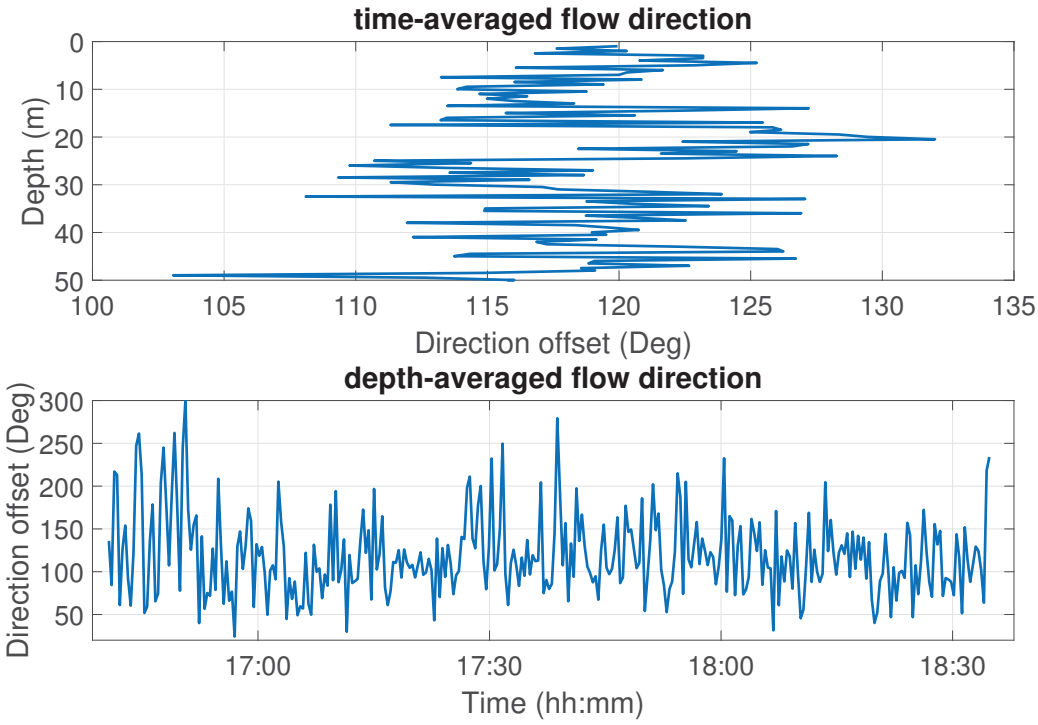

Figure 3.13: Direction of flow with relation to channel axis on day 3.

SPIRIT

SPIRIT consists of an Ultrasonic range sensor mounted to a boom equipped with an 9 degree of freedom inertial motion sensor. The sensor samples the water surface, a few meters away from the boat, with relation to itself, along with its position, pitch, roll, and yaw, relative to rest, and GPS location. By combining these data, the absolute sea surface position in space and time can be determined by the instrument. SPIRIT was recording on day 1 and day 3, collecting over 15 hours of data.

SPIRIT data provided valuable information about the surface roughness and its time scale. Figure 3.15 shows an extract of the recorded time series.

Figure 3.15 shows the wave height was roughly 0.6 m with a period of 3 sec during the short sample. The wave height seems reasonable and in agreement with visual and reported observations, but the period is slightly shorter than expected as values between 4 sec and 8 sec were reported that day.

Figure 3.14: Picture of SPIRIT during deployment.

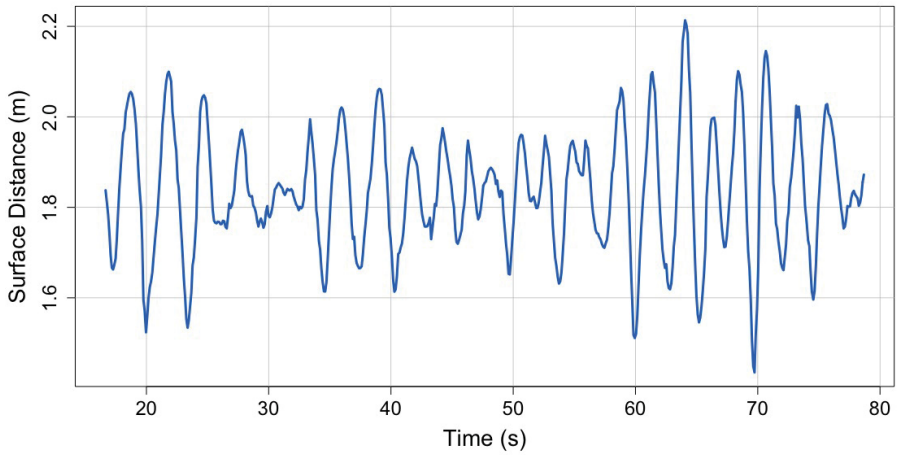

Figure 3.15: 100 sec sample of time series collected by SPIRIT.

Another validation step, shown in Figure 3.16, was to do a spectral comparison between SPIRIT's measurements and two empirical wave spectra.

During that comparison, the PM spectrum was based on the observed winds (4 m/s), and the B spectrum was matched to the peak frequency and significant wave height. The PM spectrum represents a fully developed sea in the deep ocean (Pierson et al., 1964), and B spectrum represents a one sided ocean. DalComms1 was carried out in coastal, relatively protected waters. As a result, the observed wave spectrum comprises mostly of swell, with a small contribution by locally generated wind waves.

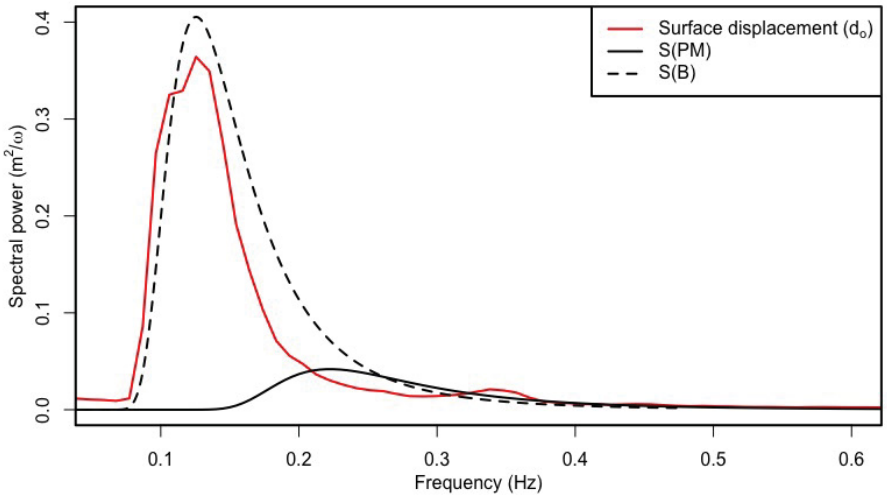

Figure 3.16: DalComms1 day 1 (July 26th) spectral comparison between ocean surface deflection (red), a Pierson-Moskowitz (PM) surface gravity wave spectrum (black), and a Bretshneider (B) one sided ocean wave spectrum (dashed).

Figure 3.16 shows that the spectrum of the data collected is similar to the B spectrum which represents a one sided, or coastal, ocean.

3.2.2 Communication setup

VLA

The receiver was a 5-element vertical line array anchored to the seabed and located at a depth of 38 m. The spacing between elements was half the transmission's wavelength or 33 cm. A summary of its parameters is shown in Table 3.3.

The receiver's depth was consistent throughout the sea trials and only varied slightly under the influence of the tides. The position of the shallowest receiver, shown in Figure 3.18, was recorded by a depth logger attached to the strength member. While not measured, it is assumed that both the source and receiver were subjected to horizontal motion during transmissions.

Figure 3.17: Picture of primary receiver's setup.

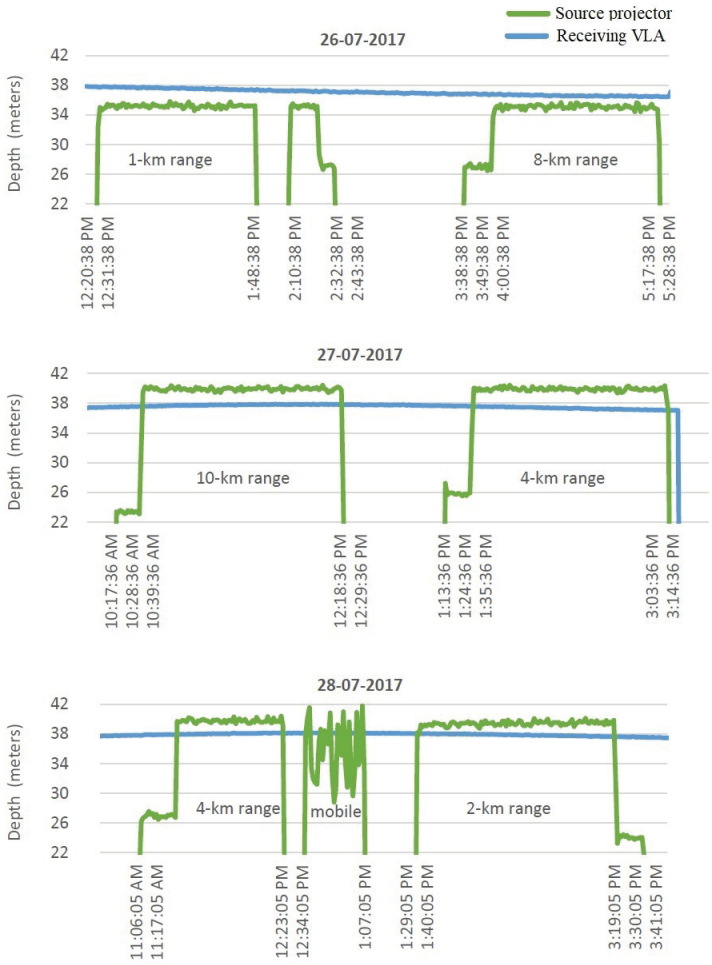

Figure 3.18: Recorded depth of the projector and receiver throughout the sea trial.

Table 3.3: Receiver and probing sequence parameters summary.

Parameter	Description	Value
f_s	Sampling rate	24000 Hz
f_c	Carrier frequency	2048 Hz
R	Symbol rate	244 Hz
OVS	Oversampling factor	42
K	Size of sequence	1024 symbols
L	Number of frames	128

Source

The source was an omni-directional flexural disc projector, also known as a bender, manufactured by GeoSpectrum Technologies Inc. and powered by a QSC PL380 Audio Power Amplifier. Its depth throughout the sea trial was also monitored with a depth sensor. Figure 3.18 shows that the source was not as stable as the receiver and moved vertically during transmissions as it was deployed from the surface vessel.

The signal sent was a PRN sequence 1024 chips long repeated 128 times. The PRN sequence was generated using a maximal-length bit sequence and displayed the ACF shown in Figure 2.7.

Before being sent across the medium via the projector, the PRN sequence was passed through a square root raised cosine filter with a roll-off factor of 0.25 and up-sampled by a factor of 42. Thereafter, the sequence was up-converted to a carrier frequency of 2048 Hz.

At the digital to analog converter (DAC), the sampling rate was 10240 Hz, yielding an oversampling rate of 5, a bandwidth of 243.81 Hz, and a frame duration of 4.2 sec.

The first transmission was done at the 8 km station with a transmit voltage of 480 V_{RMS}. To ensure a sufficient SNR, the transmit voltage was increased to 620 V_{RMS}, producing 189.2 dB re 1 μPa @ 1 m for all subsequent transmissions.

Every channel probing sequence has limitations. For a PRN sequence with the specified parameters and the signal processing method described above, the smallest resolvable delay between two taps is 0.7 ms and the longest tap delay is 458 ms. Also, the smallest Doppler shift resolvable is the reciprocal of the bandwidth, or 0.004 Hz. The last important limitation is apparent when looking at the sequence's ambiguity function as a function of delay shown in Figure 3.19. The strength needed for a tap

arrival to be differentiated from the noise is greater than the strongest side-lobe of the probing sequence used. In this case, any tap arrival with an amplitude 15 dB lower than the strongest tap may be confused for a side-lobe. -15 dB represents a ratio of 0.2 and this threshold was used to discriminate between tap arrivals and unwanted noise when analyzing TL and delay spread.

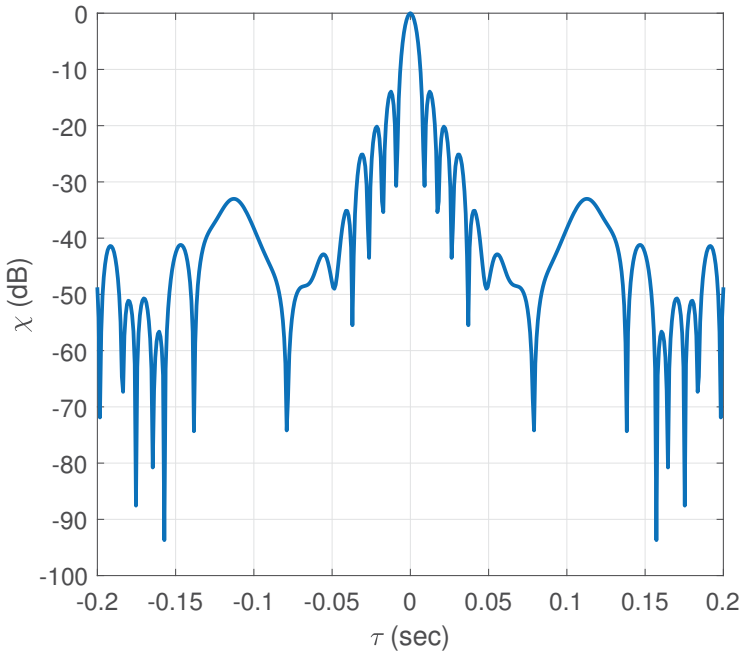

Figure 3.19: Ambiguity function as a function of delay in the absence of Doppler shift for the PRN sequence used during sea-trials.

Chapter 4

Signal Processing

In this chapter, one of the received transmissions from the DalComms1 sea trial is processed and analyzed. The analysis of this signal follows the method described in section 2.5.2. All other transmissions were analyzed and associated figures are shown in chapter 6.

The transmission analyzed in this chapter was completed on day 2. At the time, the source was held under the ship 40 m below the waterline and the receiver was 38 m deep and anchored to the seabed about 4 km from the source.

4.1 Channel impulse response and transmission loss

The sampling rate of the hydrophones forming the receiver was 24 kHz. To process the signal at the transmitted sample rate, the received signal is first down-sampled to the transmitter's sample rate of 10.24 kHz, then re-sampled at a ratio of $5003 : 5000$ to compensate for the clock-drift at the receiver. The signal is then multiplied with the carrier to bring it down to baseband and convoluted with the square root raised cosine match filter. Finally, the signal is decimated by a factor of 7 to retrieve the original pulsed-shaped sequence's sampling rate of 243.8 samples/sec.

The processed signal, $y(t)$, is then compared to the reference signal, $x(t)$, using cross-correlation. The difference between the two signals is due to the filtering and the UWAC.

The two signals are cross-correlated yielding Figure 4.1 where, from Eq. 2.30, the peaks are the first tap arrival of each 1024-chip long sequence, or frame:

As expected, the time interval between the peaks is approximately 4.2 sec, which is the frame's length. The amplitude of those peaks is dependent on the acoustic channel. In very mild conditions with no transmission loss or distortion, the received and sent signals are very similar and the cross-correlation function (CCF) will be closer to unity, whereas the CCF is much lower when the channel alters the signal

significantly.

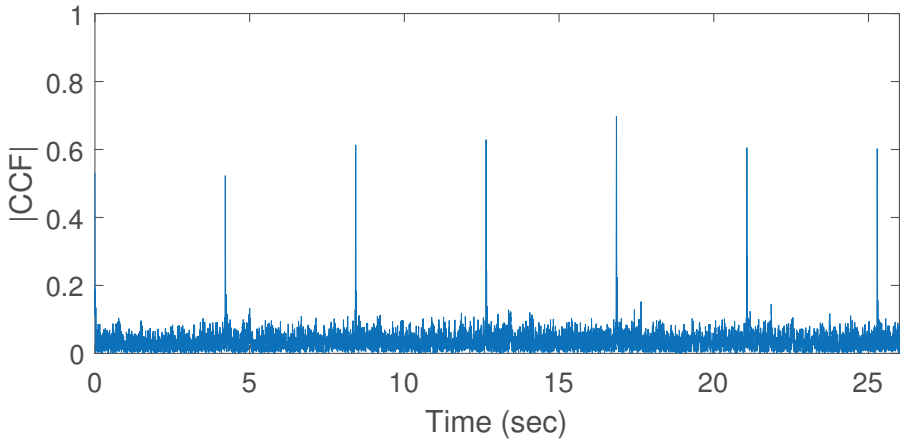

Figure 4.1: Sample of absolute value of cross-correlation function between x(t) and y(t).

Cropping the CCF into frame-length windows allows separation of the time and delay domains. Figure 4.2 shows the example of a single window with 2 strong tap arrivals due to multipath. The figure also illustrates the presence of side lobes. Two side lobes are visible before the first tap arrival and a later one is merged with what appears to be a second reflected path arrival. There may be later arrivals, but they are not distinguishable from the noise.

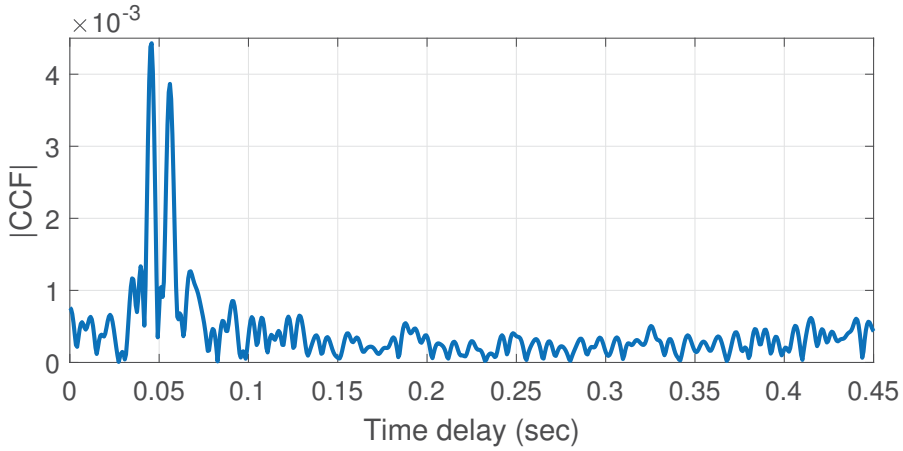

Figure 4.2: CCF for t = 3.5 min (frame 100) showing the main and secondary tap arrivals.

Figure 4.2 illustrates the CCF between the reference and received signal for a

specific frame as a function of delay. Completing the same for each frame and stacking the CCFs allows the tracking of variations with respect to time.

The normalized CCF of all 128 frames can be inserted into Eq. 2.33 to get an estimate of the CIR. Figure 4.3 shows the CIR obtained.

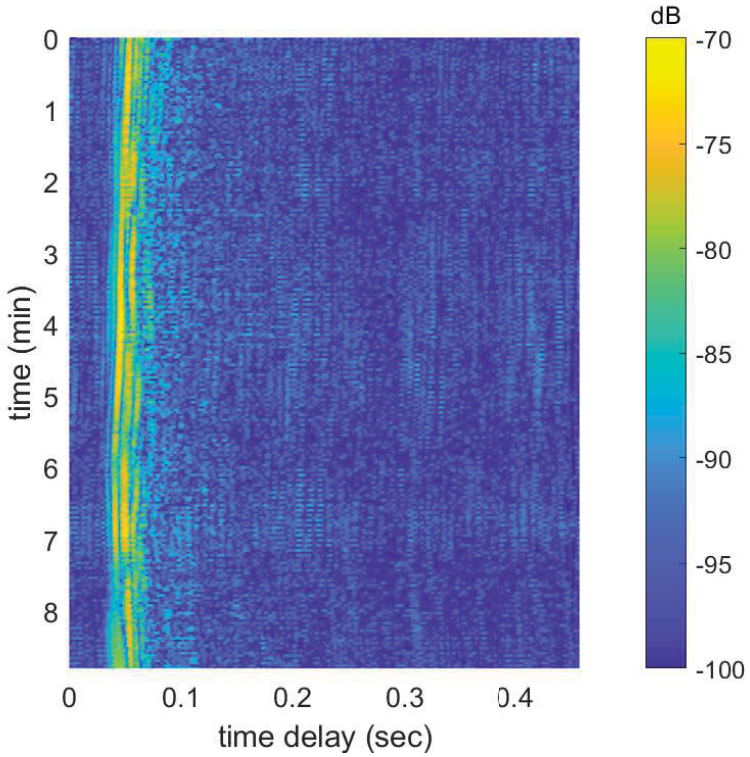

Figure 4.3: Estimate of channel impulse response (CIR) as a function of time and delay.

It is possible to distinguish the direct path arrival as well as a 1 or 2 reflected paths depending on time.

The CIR may also be investigated in the time and delay domains separately. Figure 4.4 shows the CIR as a function of time which provides the TL of the main arrival, or direct path, as a function of time for a specific time delay. In this case, the delay chosen was the one with the highest CIR amplitude which varied slightly as a function of time.

Figure 4.4 shows just under 10 mins of transmission with an average TL of 74 dB and fading reaching 83 dB on receiver #4. Accounting for all the energy received, and not solely the strongest tap, yields a TL of 62.64 dB or $17.4\log(r)$ which is

between theoretical shallow and deep water spreading loss. That result is also similar to what is expected in a shallow water environment (Urick, 1983). Overall, the 5 receivers follow the same tendency, but the TL spread is larger in the second half of the transmission. For the most part, TL increased as a function of receiver depth and the difference between receiver #1 and #5 reached over 10 dB.

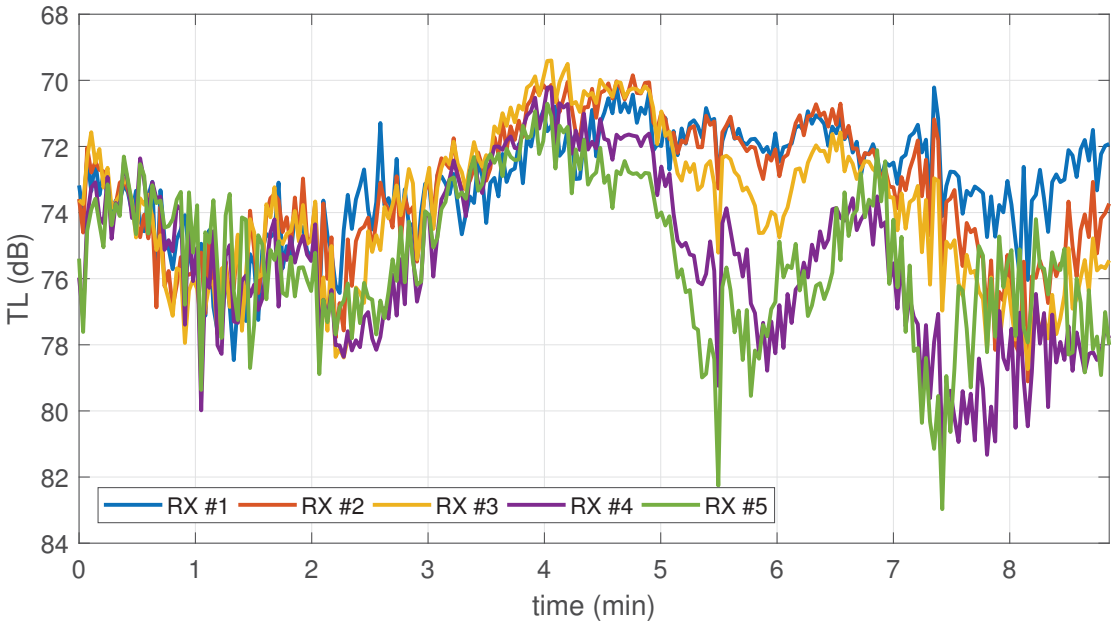

Figure 4.4: Transmission loss (TL) as a function of time for the direct path at five receivers.

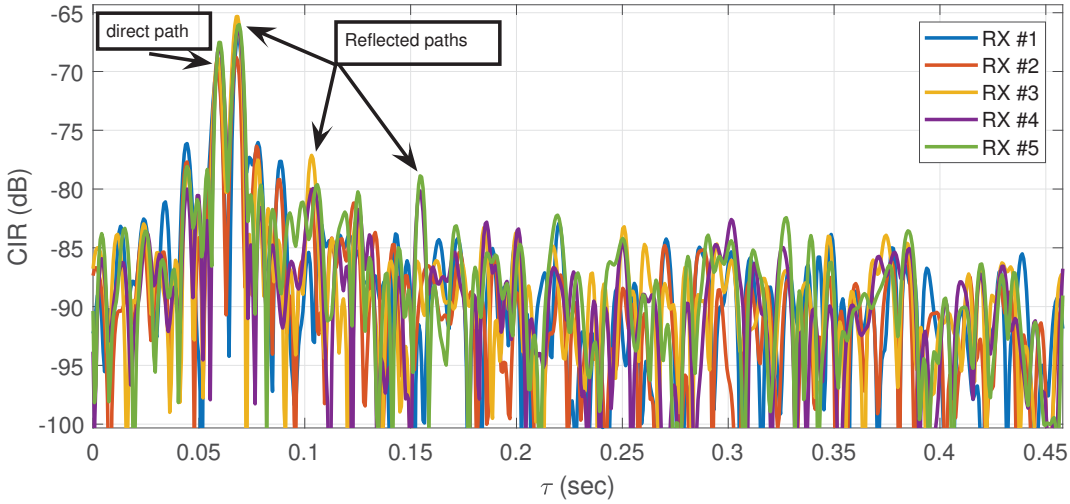

Figure 4.5: Estimate of channel impulse response as a function of delay.

Finally, Figure 4.5 illustrates the CIR as a function of delay, τ, for $t = 100$ sec.

From this plot, the direct path arrival as well as 3 reflected paths are distinguishable before the later arrivals blend into the ambient noise.

4.2 Delay and Doppler spreads

The delay between the first and last resolvable path arrival is referred to as the delay spread and it varies as a function of time. The delay spread can be used as the upper limit of integration for the RMS delay spread. Since looking at the CIR for every time step is impractical, a threshold of 0.2 times the amplitude of the strongest arrival, in linear space, was used to distinguish the tap arrivals from noise and side-lobes. Figure 4.6 shows the 5-hydrophone averaged RMS delay spread as a function of time.

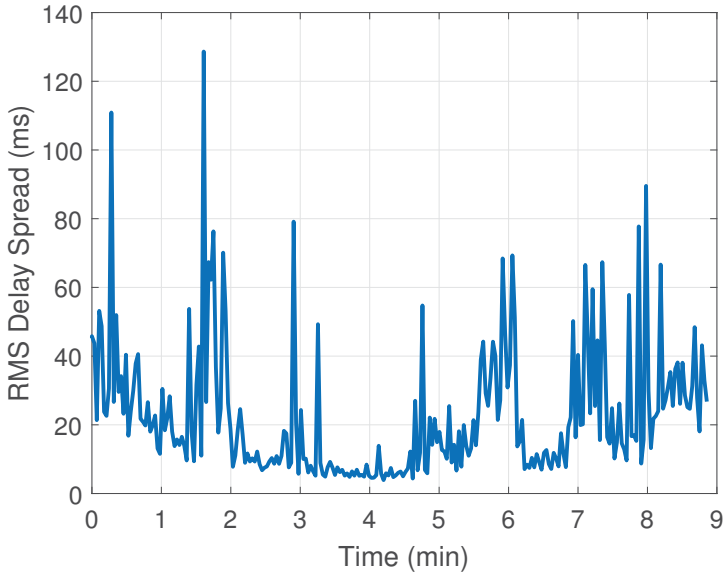

Figure 4.6: 5-hydrophone averaged delay spread as a function of time at a range of 4 km.

The delay spread mean is 22.7 msec signifying that the multipaths are spreading over tens of symbols and the fluctuations are up to six times greater than the mean. Those variations could be attributed to the changing boundaries (i.e. surface roughness) over time. The length of time over which multipath is present may impair the performances of underwater communications due to inter-symbol interference (ISI). A slower transmission rate would therefore increase the performance.

Figure 4.7 shows the probability distribution function (PDF) of the delay spread shown in Figure 4.6:

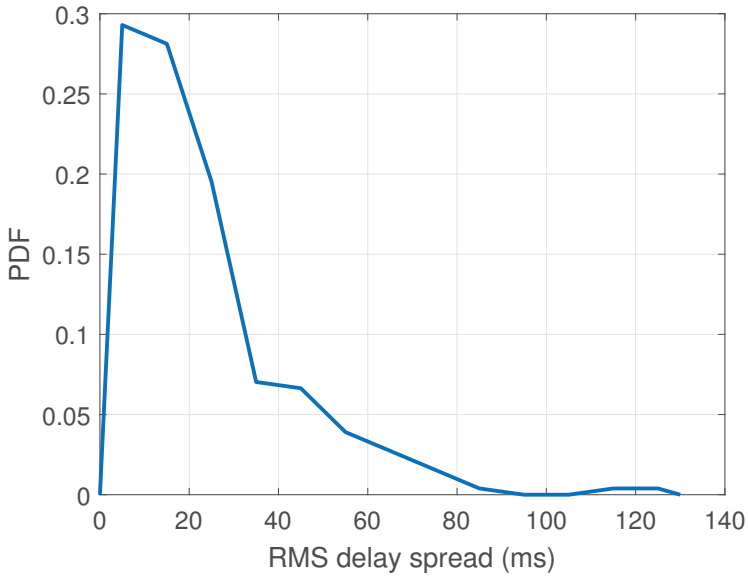

Figure 4.7: PDF of 5-hydrophone averaged delay Spread at a range of 4 km.

Despite the large variance, more than 50% of the delay spreads are below the mean. The variance may be caused by changes in sea surface and sound speed, but could also be attributed to higher than average ambient noise making it above the threshold and being recorded as a tap arrival. Raising the threshold would not be beneficial since real tap arrivals could be missed, artificially lowering the delay spread.

As discussed in section 2.5.2, a few other parameters are used to analyze the time-varying channel, two of them being the Doppler spread and the coherence time. To obtain the Doppler spread function, a Fourier Transform with respect to time must be applied to the CIR illustrated in Figure 4.3:

$$\hat{h}(f,\tau) = \int_{\infty}^{\infty} \hat{h}(t,\tau) e^{i2\pi f t} dt, \tag{4.1}$$

and the result is shown in Figure 4.8.

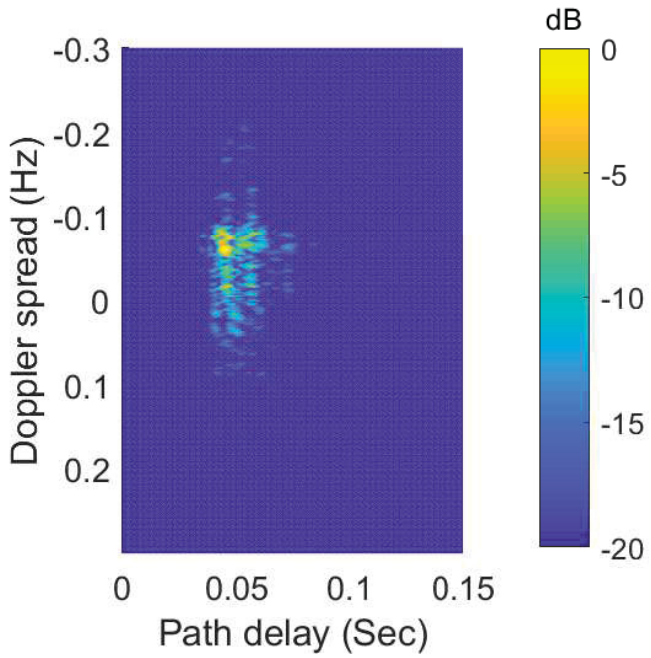

Figure 4.8: Channel impulse response as a function of frequency and path delay.

From Figure 4.8, the Doppler spread is about 0.1 Hz for all the tap arrivals. The very short time delay between the tap arrivals makes it difficult to isolate them from one another. The lack of time delay dependence also suggests that the Doppler shift is caused by something affecting all the taps, for example equipment motion, and not surface roughness. The presence of Doppler spreads on both sides of the frequency axis illustrates that the motion between the source and the receiver was not unidirectional and was most likely related to relative motion between the source and receiver due to current as opposed to the ship drifting. Using Eq. 2.36, a maximum relative velocity on the order of 4 cm/sec can be inferred. Since the Doppler spread is much smaller than the baseband bandwidth, the channel may be categorized as underspread or slowly fading.

4.3 Coherence time

The coherence time may be obtained in two ways. The first method is to analyze the CIR's ACF with respect to time. Before being able to produce such ACF, the tap arrivals in the delay domain must be summed so that the CIR is only a function of time. The summation was weighted by the Sinc function shown in Figure 4.9.

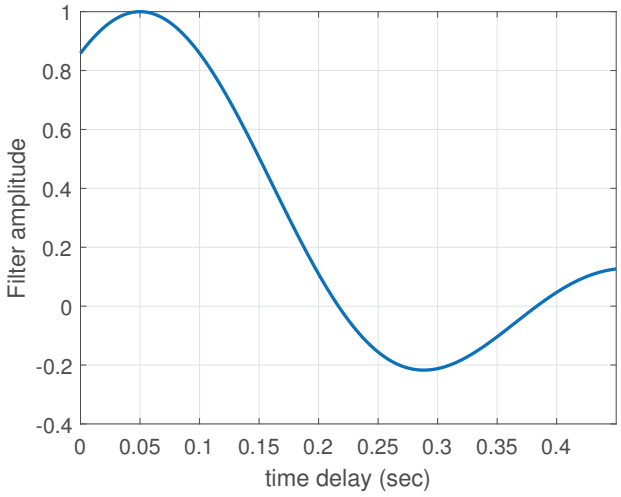

Figure 4.9: Sinc function used to sum the time delay domain of CIR.

where the maximum is located around the strongest arrival and the first zero cuts off the section of the CIR dominated by noise. This was done to limit the contribution of ambient noise and to ensure that the signal had greatest contribution possible. Figure 4.10 shows the resulting ACF:

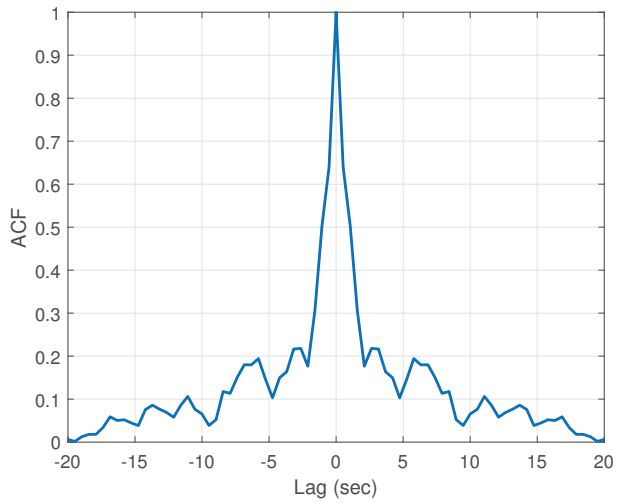

Figure 4.10: ACF of CIR with respect to time.

The definition of coherence time used during the analysis is the time required for the ACF to drop under 0.5. In this case, the coherence time of 2.63 sec is comparable to the 1.79 sec given by Eq. 2.37. Since the coherence time is much greater than

the symbol period, the channel can be considered as a slowly fading channel and the distortion at the receiver should be minimal.

Chapter 5

Simulations

This chapter describes the Bellhop modeling portion of the research. A baseline was established and compared to measurements from the sea trial. The baseline was used to select Bellhop parameters such as TL calculation method, ray density and simulation resolution. Once the parameters were set, a comparison between simulated and measured CIR was completed.

Then, a series of simulations was completed to help determine the statistical properties of the channel, focusing on TL, and to model the perturbations caused by the temporal changes of the environment. This series of simulations also provided information on the contribution of those perturbations on the variations in TL.

5.1 Baseline

A Bellhop simulation with the parameters shown in Table 5.1 was completed using the SSP taken on July 28th at 10:27 ADT and generated the results presented in Figures 5.1-5.4. The receiver depths represent the shallowest and deepest hydrophone depths recorded during the transmission. The SSP and source/receiver depths were chosen to represent the sea trial transmission at a range of 4 km. Table 5.1 summarizes to simulation parameters used.

The SSP was interpolated using a spline, and the top boundary condition was set to vacuum (default). The attenuation was expressed in dB/m/kHz and Throp's model was used to calculate the associated TL. Those parameters are represented by the SSP setting (SVFT).

Figure 5.1 shows the TL, using Thorp's attenuation and semi-coherent summation, as a function of range and depth. This scenario shows a strong direct path and a bottom reflected path bouncing approximately every 1.5 km. The surface interactions are mostly limited to the first 5 km because the source is below the thermocline and therefore, the rays tend to be refracted downwards.

Parameters & Properties	Environment file
Freq (Hz)	2048
SSP settings	SVFT
Source depth (m)	38
Receiver depth (m)	37, 38, 39
Bottom Density (g/cm^3)	2.0
Bottom sound speed (m/s)	1800
Bottom Attenuation (dB/m/kHz)	0.5
Ray density (ray/deg)	51
Ray type	Gaussian
Simulation resolution (m)	1.0

Table 5.1: Bellhop baseline simulation's parameters.

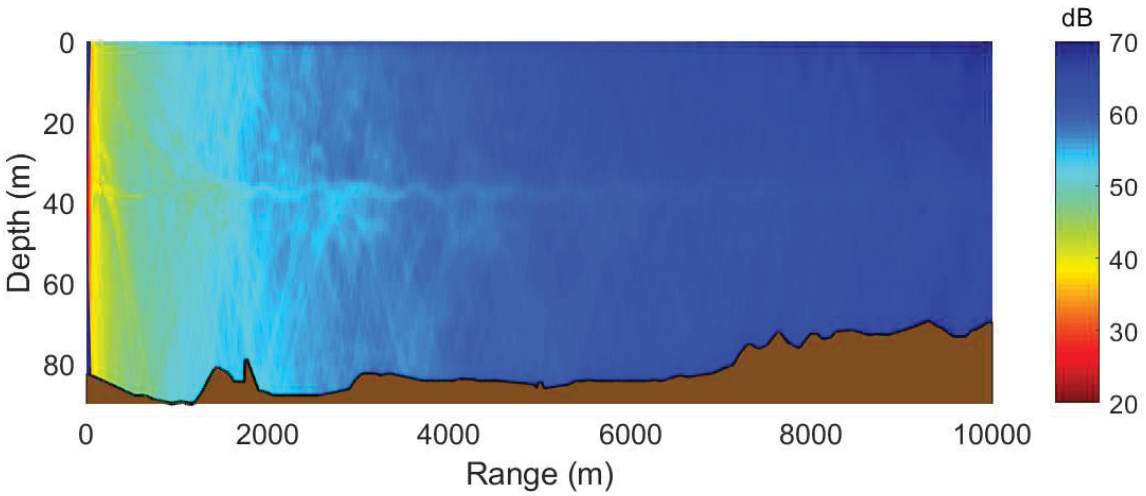

Figure 5.1: Semi-coherent TL for source at 38 m deep with bathymetry in brown.

At 10 km, the model shows a TL of about 65 dB for a receiver at 38 m deep. In comparison, the averaged TL for the 10 km transmission was 69 dB.

Figure 5.2 represents the TL as a function of range for three depths: 37, 38 and 39 m. Precision errors on the order of 1 meter in the depth of the receiver have a small, but measurable, impact on TL. Such errors may lead up to a 4 dB of variation near the receiver and just under 0.3 dB 10 km away from the source.

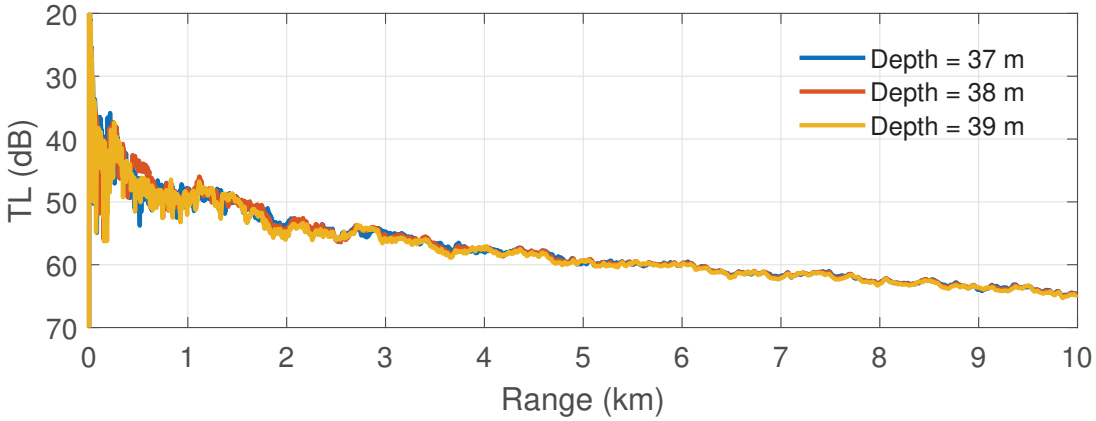

Figure 5.2: Semi-coherent TL for source at 38 m deep with receiver at 37, 38 and 39 m deep.

The choice of summation used to compute the TL has significant repercussions on the model's output. Figure 5.3 illustrates the difference between adding the rays incoherently, semi-coherently, and coherently and compares them to sea trial measurements. The incoherent and coherent calculations were completed using two methods: the built-in summation used by Bellhop and the summation of the Amp-Delay output using Equations 2.25-2.26. The main difference between the two methods is that some weaker arrivals are omitted in the Amp-Delay output, sacrificing some fidelity for smaller file size and shorter computation time. This is noticeable if comparing the curves in Figure 5.3, where the missing energy from the smaller arrivals results in higher TL for both curves calculated from the Amp-Delay file. When comparing to the measured TL, the Amp-Delay incoherently summed provides the best results. As discussed in section 2.4.1, the coherent calculations introduce hyper-realistic fluctuations and the incoherent calculation smooths the TL curve which is demonstrated in Figure 5.3. The measured TL was obtained by averaging the received amplitude in linear space of the 5 receivers before converting to dB.

Using the Amp-Delay output also allows for the extraction of the tap arrivals as a function of delay for a specified depth and range. A simulated CIR may be obtained by discretizing the channel. Figure 5.4 shows such a CIR for a receiver located 10 km away from the source, at the source's depth, superposed over a measured CIR at the same ranges and depths.

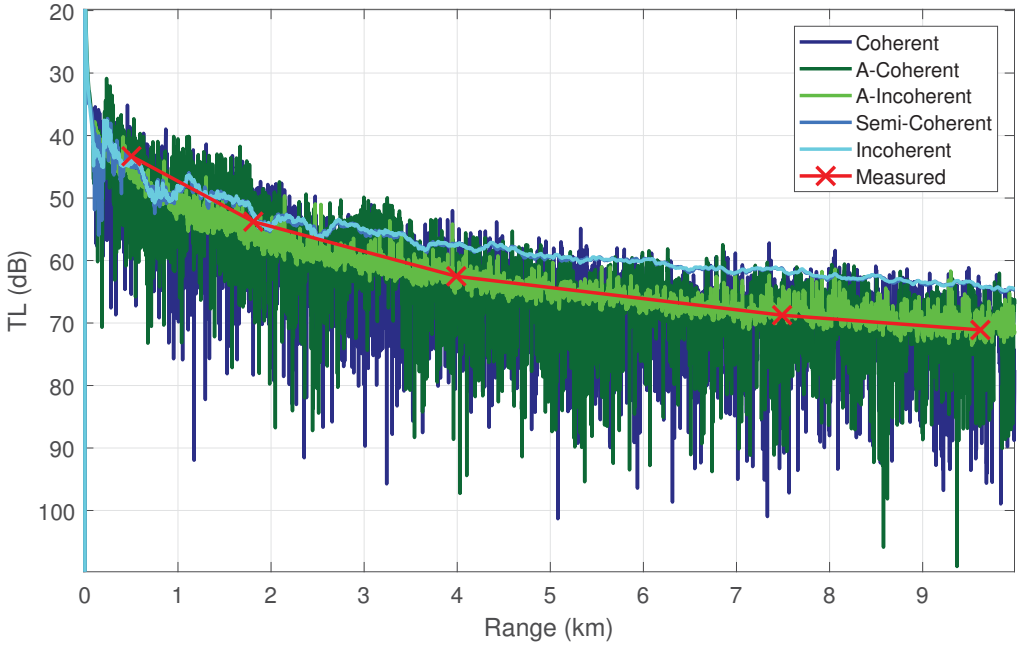

Figure 5.3: Comparison of TL as a function of range between different TL calculations and measurements. The coherent (dark blue), semi-coherent (light blue) and incoherent (cyan) TL are from of Bellhop's coherent, semi-coherent, and coherent simulations respectively. The A-coherent (dark green) and A-incoherent (green) are summed versions of the Bellhop's Amplitude-Delay output. The measured (red) TL is from a 5-hydrophone average of DalComm1's results.

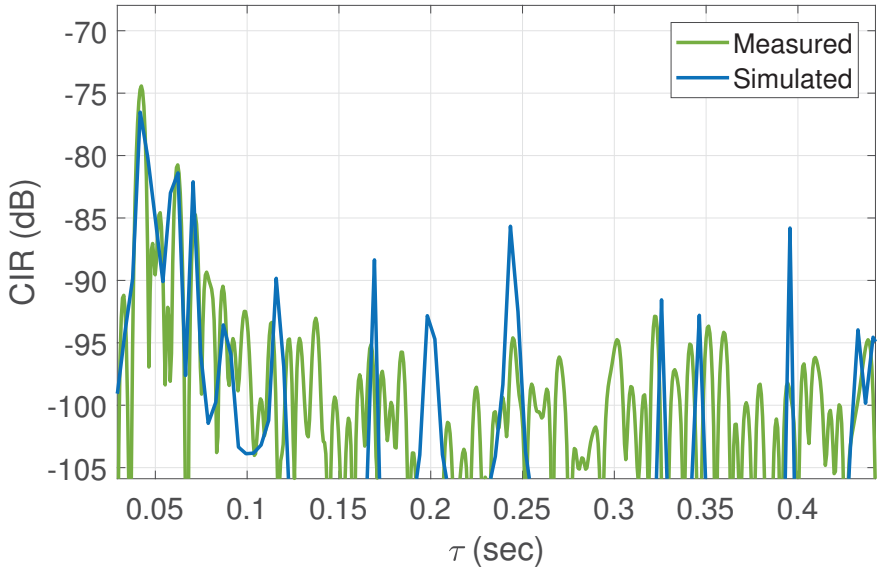

Figure 5.4: Synchronized measured and simulated CIR for a receiver at a range of 10 km and depth of 38 m.

The Bellhop simulation was completed with a beam density of 51 rays/deg and the output was normalized. Its first tap was aligned with the first tap on the measured CIR since the time of flight is not in the data. Looking at the three strongest tap arrivals, the simulated CIR is in agreement with the measured one. The later arrivals on the simulation are not represented in the measured data, suggesting that the ray-tracing model output may be superficial once the rays interact with the boundaries at multiple occasions. This could be due to the lack of high resolution data for the bottom boundary, including bottom properties and bathymetry, the lack of accuracy in sea surface and the lack of time-variant channel simulation.

5.2 Time-variant and uncertainty analysis

Bellhop provides a deterministic solution and therefore does not model channel time-variability. To investigate the variability seen in the measurements, as illustrated in Figure 4.4, further simulations with varying rough surface realizations, SSPs and bottom properties were completed. The objective was to determine which physical properties have the most significant impact on the acoustic channel and how they affect TL variability. Furthermore, the precision error in the position of the source and receiver was studied by looking at the received signal within a box around the estimated position of the receiver.

The TL was calculated for 3 different receivers:

1. Single-point receiver (orange): The receiver is a 1x1 m square (simulation's resolution) placed at 38 m below the surface;

2. Box-averaged receiver (blue): The receiver is a 9 m long by 5 m tall box centered on the point receiver. The average of all TL within the box is used as the TL; and

3. Box receiver (green): The receiver is the exactly like the second receiver, but no averaging is done. This yields 45 TL values per receiver.

The box size was chosen to represent a realistic range of motion relative motion between the source deployed from the vessel and the VLA receiver 45 m away from its anchor on the seabed. Figure 5.5 illustrates such receivers.

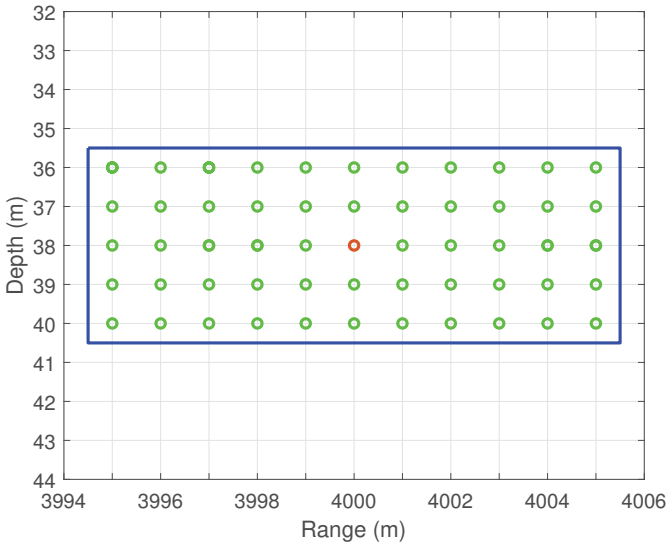

Figure 5.5: Depiction of receiver types: single-point (orange), box (green) and box-averaged (blue) for the 4 km range.

The following parameters, shown in Table 5.2 remained constant across all simulations:

Parameters & Properties	Environment file
Freq (Hz)	2048
SSP settings	SVFT
Source depth (m)	38
Receiver depth (centered) (m)	38
Bottom Density (g/cm^3)	2.05*
Bottom sound speed (m/s)	1800*
Bottom Attenuation (dB/m/kHz)	0.5*
Ray density (ray/deg)	51
Fan width (deg)	-40/+40
Ray type	Gaussian
Simulation resolution (m)	1.0

Table 5.2: Bellhop ensemble simulation's parameters.

* Except during the bottom properties ensemble.

5.2.1 Design of the ensembles and results

The following section focuses on the 4 km range is divided into: design of the simulation ensembles & results and delay spread.

Surface ensemble

The impact of the evolution of the rough surface over time was studied using an ensemble of simulations. A 100 different surface realizations were generated using the spectral density function obtained by SPIRIT and a MATLAB toolbox called Wave Analysis for Fatigue and Oceanography (WAFO). Each simulation used a different sea surfaces, but all realizations were from the same wave spectrum (Figure 3.16).

The resulting TL PDF for a receiver 4 km away from the source is shown in Figure 5.6.

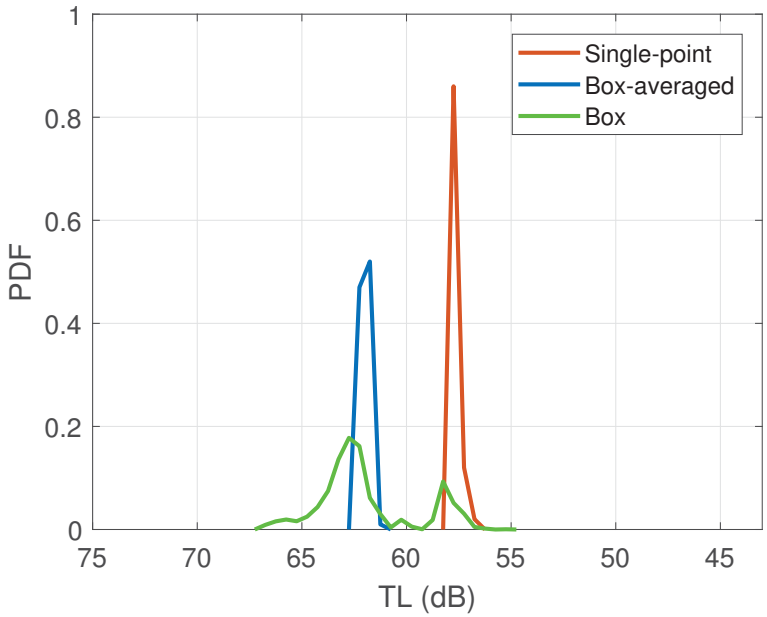

Figure 5.6: PDF of TL for the surface ensemble at a range of 4 km.

The first noticeable feature is the PDF for the single-point receiver shown in orange. In this case, the environment and receiver location yielded a TL of 58 dB which is not representative of the TL in its near proximity (within the box receiver) averaging 63 dB.

The green PDF represents the TL computed at every point in the box and illustrates how individual receivers may be outliers, and, if chosen inadvertently, could provide poor fidelity. From that curve, we can conclude that motion at the receiver or an error in position of a few meters can lead to a 12 dB spread.

Looking at the static receiver, or single-point receiver, the impact of the changing

surface alone is less drastic showing a 1.5 dB spread.

Sound speed profile ensemble

The impact of SSP variations on underwater communication was investigated by running 100 Bellhop simulations, each with a slightly different SSP. The time interval between the 70 SSP collected led to variations much greater than what was observed on a 9-min transmission time scale. Therefore, a few CTD casts taken in a short period of time (within 45 mins) were used to generate a larger number of similar SSPs. The SSPs used were generated from measured CTD data using the following procedure:

1. the PDF of the depth rate of change of the SSP was estimated from the measured data, over the entire water column;
2. the sound speed at the surface was randomly chosen between the minimum and maximum surface sound speed from measured data;
3. subsequent, or deeper, sound speeds were calculated by taking the previously sound speed and adding a rate of change that follows the measured PDF for that specific depth; and
4. the divergent profiles were removed.

The result is a relatively smooth, measured-like profile lying between the most extreme measurements. Such SSPs are compared to measured profiles in Figure 5.7.

For the SSP ensemble, the CTD measurements made at the 8 km station were used because that time period has the highest amount of CTD cast density. As a result, 7 SSPs measured within a 45 min interval were used to replicate changes occurring on a reasonable transmission timescale. The temporal resolution of the measurements remains low and aliasing of faster fluctuations is likely happening. This SSP generation method is an attempt to capture those.

The resulting TL PDF for a receiver 4 km away from the source is shown in Figure 5.8.

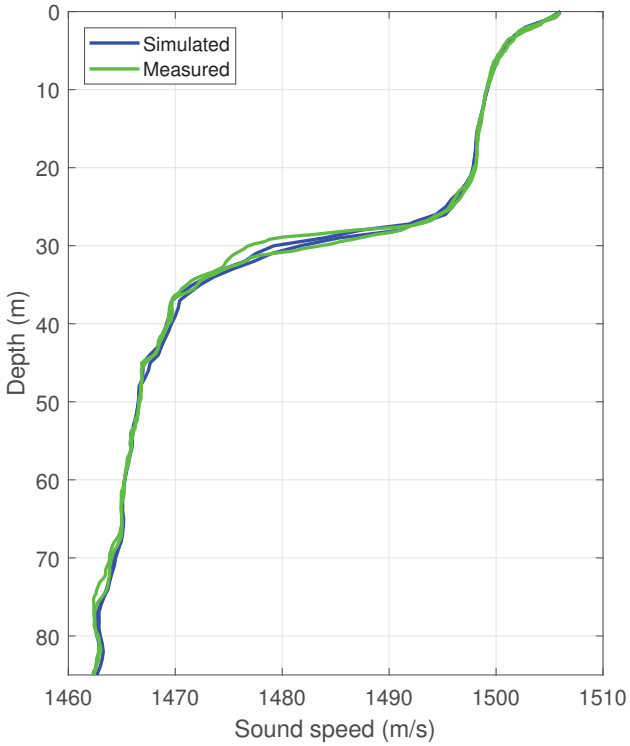

Figure 5.7: Comparison between two randomly generated and two measured SSPs.

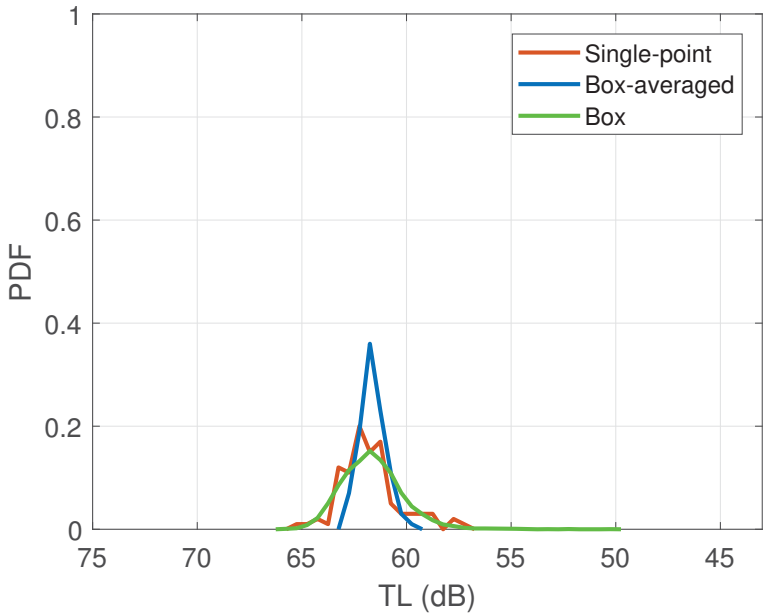

Figure 5.8: PDF of TL for the SSP ensemble at a range of 4 km.

In the ensemble, the three types of receivers display similar PDF shape, mean and variance. These similarities seems to be due to the impact of the changing SSPs being greater than or equal to variations caused by the position of the receiver within the box. A spread of 3 dB is observed when looking at the box-averaged (blue) however the spread increases to 10 dB when looking at all the receivers in the box. The large spread of the single-point receiver and its similarity to the box receiver may be because the SSP variations do not change the total amount of TL within the box, but change where the strong path crosses the box (more on this in section 6.2).

Bottom properties ensemble

For underwater communication timescales, the bottom composition is unlikely to change and, therefore, the ensemble is not used to look at time-variance. Instead it is used to investigate the impact of uncertainty in measurement or in the estimation of bottom properties. This ensemble looked at the impact of sound speed and attenuation in the sediments. The attenuation was varied between 0.1 and 0.8 dB/m/kHz with steps of 0.05 dB/m/kHz. The sound speed varied between 1730 and 1850 m/s with steps of 8.5 m/s for a total of 225 simulations. Those ranges were chosen because they represent realistic values on the Scotian shelf, while being large enough to cover a wide variety of bottom types. The ensemble allowed to compare the impact of attenuation versus the sound speed in the bottom as shown in Figure 5.9.

The figure above is representative of the results across all ranges and shows that the estimation error in bottom attenuation values has a greater impact on resulting TL than bottom sound speed errors. Change in bottom sound speed resulted in TL variation of less than 0.3 dB, while the TL variation caused by a change in attenuation value reaches 2.5 dB. Despite the fact that accuracy in attenuation is more important than bottom sound speed, its impact remains limited since a large change in attenuation value leads to a moderate TL variation. This is most likely due to the low carrier frequency and the short range between the source and receiver.

The resulting TL PDF for a receiver 4 km away from the source is shown in Figure 5.10.

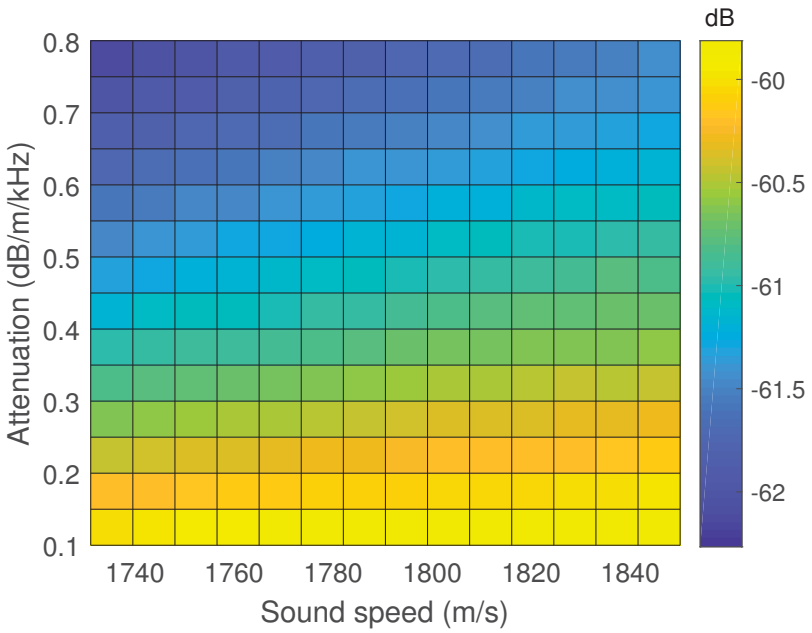

Figure 5.9: TL as a function of bottom attenuation and sound speed for a point receiver at 4 km.

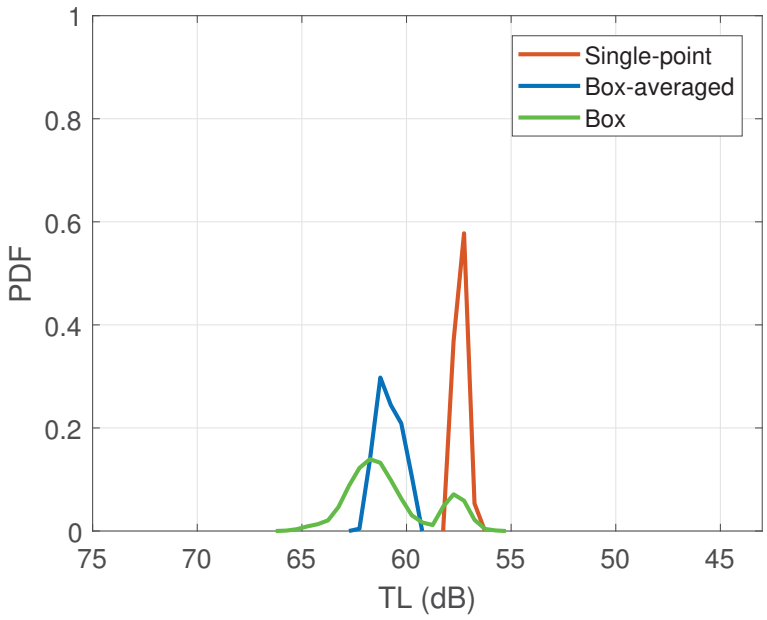

Figure 5.10: PDF of TL for the bottom ensemble at a range of 4 km.

The single-point receiver differs 3.5 dB from the average and its spread is approximately 1.5 dB. Figure 5.10 is similar to what was seen with the rough surface ensemble in Figure 5.6 and, again, the motion has the larger impact (a few dB) than

the changes of bottom properties on TL variation.

5.2.2 Simulated delay spread

The unique nature of each run provides a unique impulse response as a function of time delay (i.e. eigenrays have different delays and amplitudes for each simulation). Therefore, each simulation has a different delay between first and last tap arrival, or delay spread. The mean, variance and overall PDF of the RMS delay spread can be calculated and compared against the measured values. Table 5.3 summarizes the results.

Ensemble	Mean (ms)	Variance (ms^2)
Rough surface	12.0	12.5
Sound speed	37.7	61.3
Measured	22.7	368

Table 5.3: RMS delay spread mean and variance as a function of ensemble in milliseconds.

The rough surface ensemble has a much lower delay spread compared to the SSP ensemble. A possible explanation for this is that the rays are mostly refracted downwards and interactions with the surface is limited.

While the mean of the simulated results is within a factor of 2 from the measurements, the simulated variance is not representative of the measurements. Figure 5.11 shows a PDF comparison between measured and simulated delay spread values for the 4 km range.

The delay spreads generated by the simulated data have a Gaussian distribution where the PDF is centered on the mean and its spread is approximately 6 standard deviations. The PDF from the measured data has a strong left bias and a long tail on the right. One explanation is that presence of noise in the measured data adds a source of complexity and it is possible that some noise is mistaken for later tap arrivals.

One may come to the conclusion that the RMS delay spread generated by the surface and SSP ensemble are a rough estimation of the measured data, but it does not capture the difficulty of differentiating late arrivals from noise.

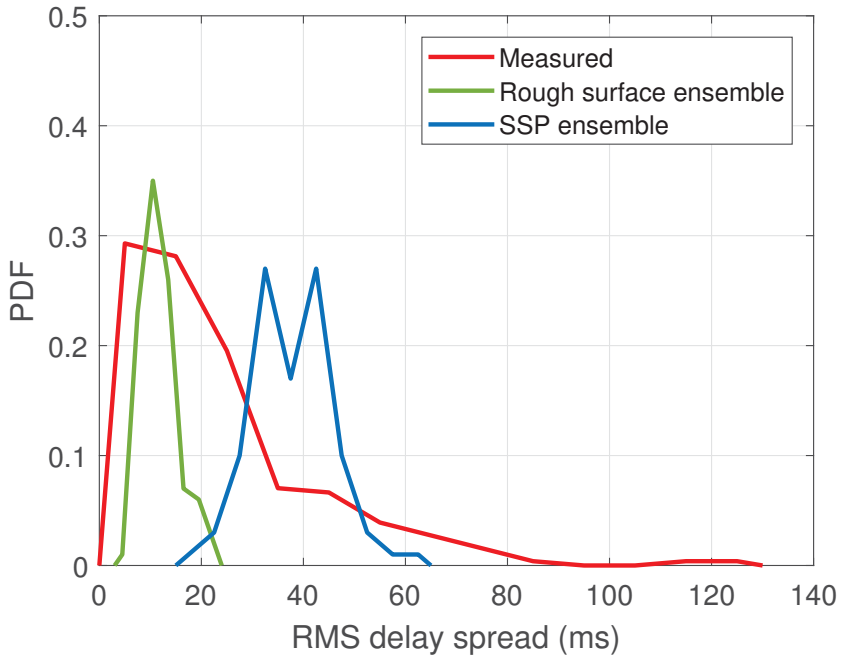

Figure 5.11: PDF of RMS delay spread at 4 km for the measured (red) data, surface ensemble (green) and SSP ensemble (blue).

Chapter 6

Discussion

This chapter elaborates on the signal processing findings and compares them across all ranges. It also discusses the results from the simulations ensemble and compares them to those observed during the sea trials. The last section contains the reasoning behind assumptions taken during the analysis.

6.1 Signal processing

One of the most informative figures is the CIR since it provides an overview of the TL, the severity of the multipath and the time-variability of the channel. Figure 6.1 shows the estimated CIR for all ranges. At a range of 2 km the received signal has 2 strong arrivals for most of the transmission's duration. At a range of 4 km the received signal has between 2 and 3 strong arrivals changing on a minute-long timescale. Beyond that range, the number of arrivals varies greatly as a function of time.

From the data in the figures above, the channel varies significantly over time. The strength of the strongest tap arrivals fluctuates by over 10 dB in all transmissions. Furthermore, the number of taps and the amount of delay spread also change over time, especially during the 8 km and 10 km transmissions.

Table 6.1 contains the coherence time observed at sea. In shallow water, the coherence time is strongly dependent on wind speed (Badiey et al., 2000) and this is noticeable in the results.

	2 km	4 km	8 km	10 km
Coherence time (sec)	2.63	1.05	2.1	3.16

Table 6.1: Coherence time for all transmissions.

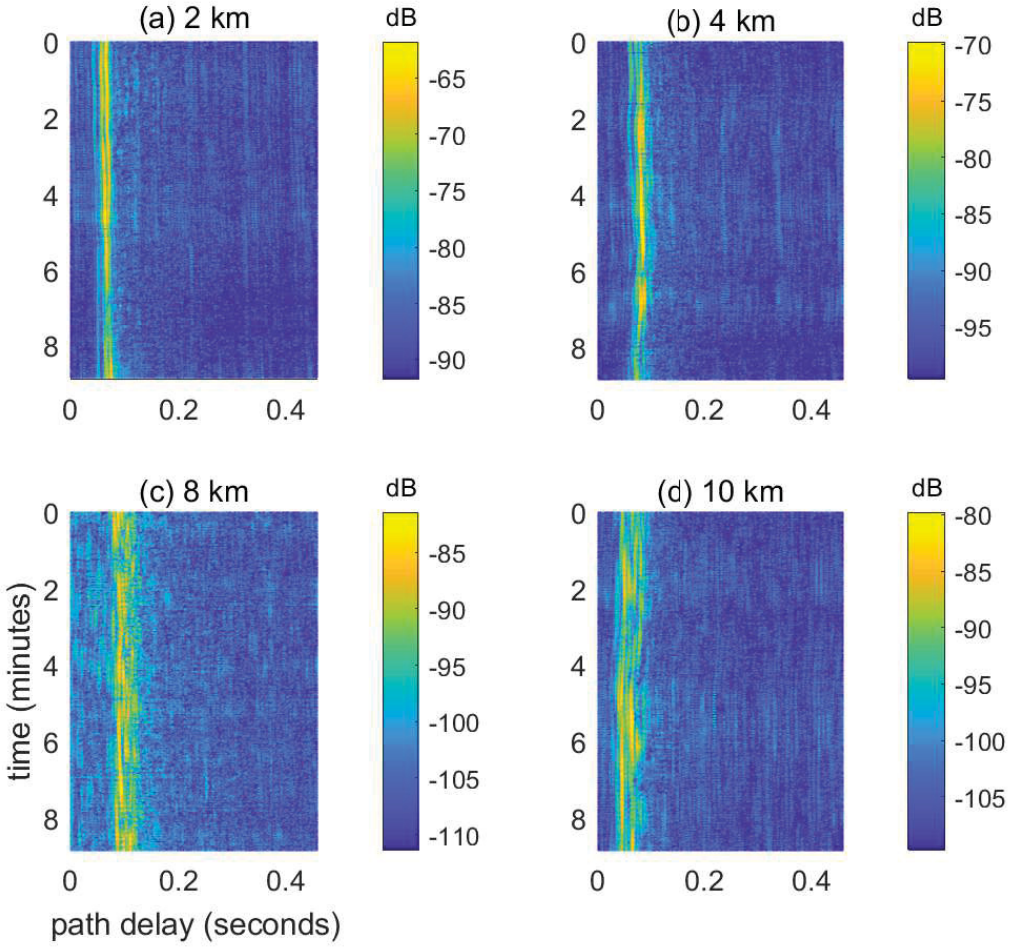

Figure 6.1: Estimated CIR as a function of time and path delay for ranges of 2 km (a), 4 km (b), 8 (c) and 10 km (d).

Table 6.2 contains average wind speed and significant wave height for each transmissions.

	2 km	4 km	8 km	10 km
Wind speed/gust (m/s)	3.0/3.0	6.0/7.0	6.0/8.0	4.0/5.0
Sig. wave height (m)	0.6	0.6	1.1	0.6

Table 6.2: Averaged wind speed and significant wave height observed during transmissions.

The transmissions at 2 and 10 km, completed during wind speeds between 3 and 5 m/s, had the highest coherence time. Transmissions from 4 and 8 km were carried out while the wind speed reached 8 m/s and resulted in a lower coherence time.

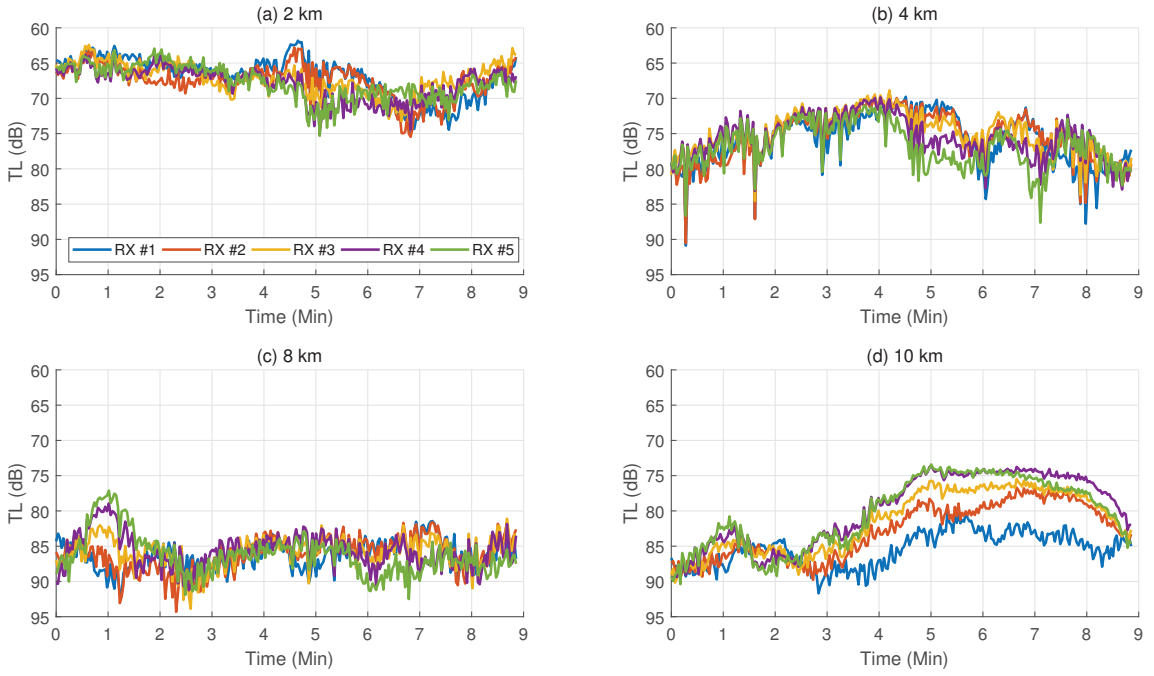

Figure 6.2: TL of strongest path arrival as a function of time for ranges of 2 (a), 4 (b), 8 (c) and 10 (d) km.

Figure 6.2 shows the TL of the strongest path arrival for the 5 receivers on the VLA. Most of the time, the 5 received signals behave similarly, with variations on short timescales of less than < 10 sec and longer timescales of a few minutes. For most ranges, the longer timescale deviations have a spread of approximately 10 dB during the 9 min transmissions.

During the 10 km transmission, a larger variation in received level between the 5 receivers was observed. In this case, a separation of 30 cm between the receivers lead to up to a 5 dB difference. This illustrates the low spatial coherence between the receivers.

The TL of the strongest tap arrival is estimated well by $20\log(r)$ across all ranges, with the exception of the 8 km range which has a higher TL than expected. When accounting for all the energy received, the TL at 2, 4 and 10 km follow a constant logarithmic increase and brings the relationship between TL and range closer to $17\log(r)$.

Tables 6.3 summarizes the delay spreads obtained through signal processing. Intersymbol interference is expected since the average delay spread is much greater than the symbol period. It is difficult to assess whether increasing the range correlates or

not with higher delay spreads due to the low number of ranges and the low value observed at 10 km. As discussed in section 4.2, it is difficult to distinguish weak arrivals and noise. This may be the cause for the high variances observed.

	2 km	4 km	8 km	10 km
Mean	15.2	22.7	38.4	17.7
Variance	103	368	164	103

Table 6.3: RMS delay spread mean (msec) and variance ($msec^2$) as a function of range.

The observations made in section 4.2 are valid across all ranges. The delay spreads from the surface roughness ensemble are always lower than those from the SSP ensemble. The simulated delay spreads are within a factor of 2 from the measured values and the variances are not representative of the measurements.

Figure 6.3 shows the Doppler spread for all transmissions. For the most part, the Doppler spread is very low and the UWAC is considered slowly fading.

Accounting for most metrics, the 8 km transmission appears to have suffered from the most challenging UWAC. It showed higher than expected TL, higher delay spread and, lower coherence time than all other transmissions. The lower performance may be explained by lower SNR due to the lower transmit power, but also the higher ambient noise caused by the higher wind speed. The transmission was also completed during the quickest deepening of the mixed layer and SSP changes had an impact.

The channel changes over time and a single ray-tracing simulation cannot provide a complete picture. Most of those changes appear to be due to changes in surface roughness induced by the wind and sound speed changes (i.e. change in mixed layer depth). Investigating the impact of those parameters by varying them over a multitude of simulation can provide a more accurate estimate of TL experience during a transmission via the UWAC.

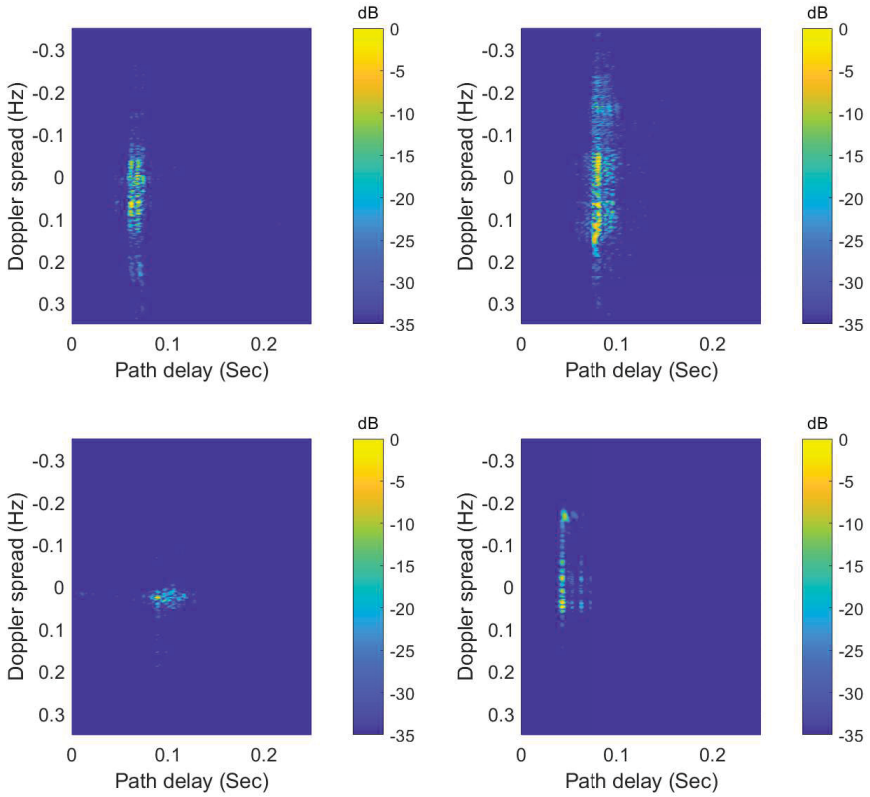

Figure 6.3: Doppler spread as a function of path delay for ranges of 2 (top left), 4 (top right), 8 (bottom left) and 10 km (bottom right).

6.2 Simulations

The baseline simulation helped make important decisions about the simulation parameters such as resolution, number of rays, and ray summation type. The amplitude-delay output was chosen because it represented the measured TL well and provided the most flexibility of all Bellhop outputs. A resolution of 1 m provided a good balance between accuracy and computation speed.

The baseline also showed that running a single simulation with a measured SSP and an estimate of bathymetry and bottom properties produces acceptable estimates of TL and CIR as a function of delay for the first three path arrivals.

The different ensembles of simulations provided insight into the factors that influenced variance in the TL measured during the sea trials most significantly. Figure 6.4

is an overview of PDFs for all ensembles at all ranges, to highlight commonalities and differences between runs.

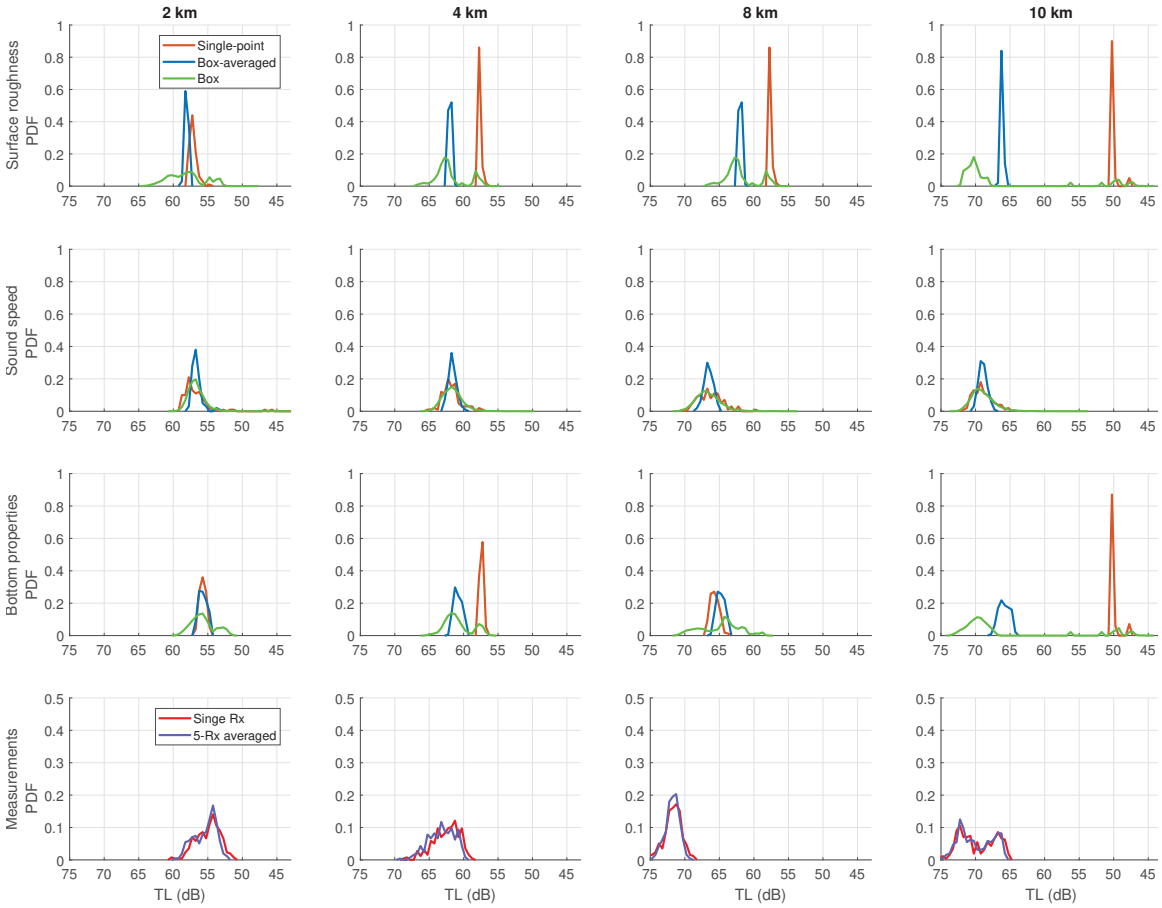

Figure 6.4: PDF of TL for single-point receiver (orange), box-averaged receiver (blue) and box receiver (green) for rough surface ensemble (first row), SSP ensemble (second row), bottom properties ensemble (third row) and measurements (last row) at ranges of 2, 4, 8, and 10 km (left to right).

The orange line represents the single-point receiver and its PDF is only influenced by the changing parameter within each ensemble. How its shape changes across range (columns) reflects the range dependence and how it changes across ensembles indicates which parameters have a greater impact on the TL deviation.

The blue line represents the PDF of the box-averaged receiver, or the mean TL within the 9x5 m box receiver. The effect of range on TL is noticed by the its PDF shifting to higher values on the x-axis. Its shape is influenced by the physical

parameter varied in the ensemble, but also the by the spatial deviation around the point receiver modeling the position uncertainty of the source receiver pair. Therefore, the difference in shape between the PDFs of the box-averaged receiver and the single-point receiver may be due to a moving receiver or simply a lack of precision in the receiver's location.

The green line shows the PDF of the box receiver without averaging. It has the same mean as the box-averaged receiver, but its spread and shape are often different. It showcases outliers and helps explain subtleties not visible in the other 2 PDFs by presenting the entire picture.

To provide some physical context, the single-point receiver represents a static receiver. The other 2 receivers represent a system where relative motion between the source and receiver is present and its range is approximately the size of the box. The box-averaged receiver models a system where the receiver moves or samples the entire box quicker than the duration of the sequence (4.2 sec during DalComms1) and the box receiver models a system where the motion is much slower than the sequence duration.

The last row is comprised of two lines, the red line represents a single receiver and the purple line shows the ensembled results from all 5 receivers on the VLA.

The first and third row of Figure 6.4 illustrates the PDFs from the rough surface and bottom properties ensembles respectively. The results for both ensembles are very similar. Looking at the single-point receiver, both ensembles generated small TL variation showing that errors in bottom properties and variations in the sea surface have little impact on TL. Range had a limited impact due to the relatively short ranges limiting the number of interactions between rays and boundaries, but the position of the receiver had a large impact on the box receiver distributions. The offset between the single-point and box-averaged PDFs as well as the bi-modal characteristic of the box PDF is explained by Figure 6.5 which represent a Bellhop simulation using the same SSP as both ensembles.

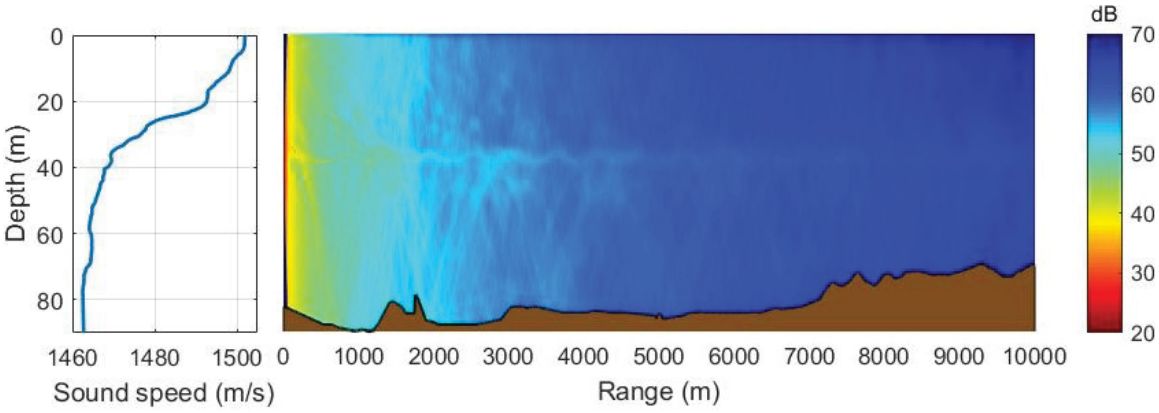

Figure 6.5: TL for source at 38 m deep with bathymetry in brown.

The strong thermocline just above the source and receiver acts as a duct trapping the direct path. The reflected paths bouncing off the bottom are also refracted down by the thermocline and contribute to the a stronger intensity in the sound field by creating a turning point at that depth for all bottom reflected, upward traveling rays. Therefore, this specific SSP, and all SSPs with a similarly strong thermocline, causes a strong path, at around 38 m deep, to cross the center of the box receivers. The result is strong point receiver and weaker amplitudes above and below it. This explains why the single-point TL, despite being in the middle of the box, has lower TL than the average. This also explains the bi-modality in the box receiver PDFs. The lower TL peak is associated with the single-point receiver and represents the strong path, while the second peak represents points above and below. This phenomenon is not present in the SSP ensemble because different SSPs raise and lower this turning point at the base of the thermocline, spatially smoothing the peak TL across depth. Therefore, the high level of similarities between the two ensembles is due to the fact that both ensembles use the same SSP. This illustrates the importance of the SSP in the determination of the TL. It also shows the importance of receiver depth to optimize performance.

The second row shows the results from the SSP ensemble. Changes in SSP produce a TL spread of approximately 10 dB. The position of the receiver is still important in this ensemble, but the similarities between the single-point receiver and box-averaged receiver PDFs suggest that the SSP is the biggest driver of TL deviations. The tail on the box receiver PDF illustrates that there are outliers within the box and choosing

them blindly to estimate performance could be misleading.

Lastly, the bottom row shows the PDF of the measured TL. The similarities between the single-point receiver and the box-averaged receiver results show that the vertical separation (33 cm) had a small but noticeable impact. The spread is on the order of 10 dB which is higher than all the variables except receiver position. Again, looking at the sea trial results, range did not have an important impact on TL variance.

The discrepancies between the box-averaged receiver and the single-point receiver for the rough surface and bottom properties ensembles illustrate how choosing a single point in the field may not be representative of the very close neighborhood. Those two ensembles share the same SSP and the similar environment led to a single-point receiver landing at one of the extremes of the PDF. Without looking at the neighboring points, the TL extracted may be over 15 dB away from the average.

Overall, range was not a big contributor to TL variance. The receiver position and SSP variations had the biggest impact. The receiver position uncertainty generated spreads of up to 30 dB within the box for the cases of 10 km, box receiver, rough surface ensemble and bottom properties ensembles. More generally, SSP ensemble simulation with all types of receiver are able to generate 10 dB of TL variance, consistent with the observations. The surface ensemble generated low, but measurable, TL variance. Its low impact can be attributed to the fairly mild sea state condition used to generate the ensemble as well as the SSPs favoring downward refraction. Uncertainty in bottom properties estimation can also lead to a measurable difference in TL of up to 1 dB.

When comparing the mean, variance and overall shape of the PDFs from simulations and those from the sea trial, we can see that no single property can account for the variance of the measured data. More likely, the variance observed during the sea trial comes from a combination of physical properties varying over time on a multitude of timescale. One can also conclude that accounting for motion at the receiver is needed to explain the variance observed in the measurements.

Table 6.4 and 6.5 show the mean and spread of the PDFs above.

Ensemble/ Range	Receiver	2 km	4 km	8 km	10 km
Surface	Point	57.1	57.6	65.8	45.0
	Box	58.1	62.0	65.3	66.2
Sound Speed	Point	56.6	61.8	66.3	68.9
	Box	56.6	61.6	66.6	69.0
Bottom	Point	55.7	57.4	65.7	49.9
	Box	55.7	60.8	64.8	65.9
Measured	Single Rx	55.0	62.5	71.7	69.7
	5-Rx averaged	55.4	63.2	71.8	69.9

Table 6.4: TL mean as a function of ensemble and range in dB.

Ensemble/ Range	Receiver	2 km	4 km	8 km	10 km
Surface	Point	0.28	0.04	0.22	0.30
	Averaged	0.05	0.01	0.01	0.01
	Box	8.09	7.09	10.0	38.2
Sound Speed	Point	6.83	2.03	3.26	2.02
	Averaged	0.21	0.16	0.21	0.18
	Box	2.26	2.16	3.22	2.77
Bottom	Point	0.21	0.05	0.40	0.41
	Averaged	0.42	0.39	0.48	0.95
	Box	2.66	4.73	9.09	37.0
Measured	Single Rx	2.96	3.64	1.58	6.77
	5-Rx averaged	2.66	3.53	0.98	6.07

Table 6.5: 3x standard deviation of the TL as a function of ensemble and range in dB.

The means generated by the box receivers are all within 4 dB of those measured and in most cases, this falls within the spread (estimated by 3 standard deviations) of the measured TL. Therefore, the ensemble have a reasonable degree of fidelity with respect to the average TL.

Another way to represent the data is to look at TL as a function of range with upper and lower limits representing 3 standard deviations. Such figures could be used to obtain an expected best and worst case scenario when designing an at sea deployment.

Figure 6.6 shows the spread caused solely by the varying rough sea surface. Its contribution to TL deviation is measurable, but much smaller than those of SSP and motion.

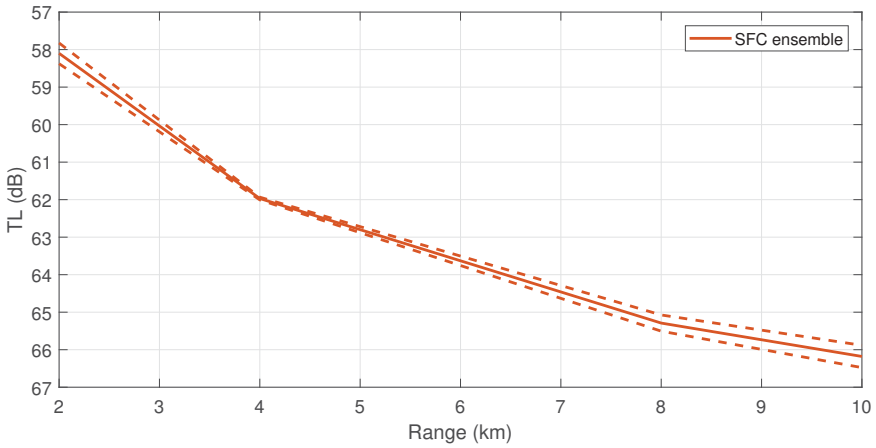

Figure 6.6: TL for SFC ensemble with 3 standard deviations.

Figures 6.7 and 6.8 illustrates the box receiver and its deviation compared to the measured TL and shows, again, that the ensembles are a good estimate of the measurements.

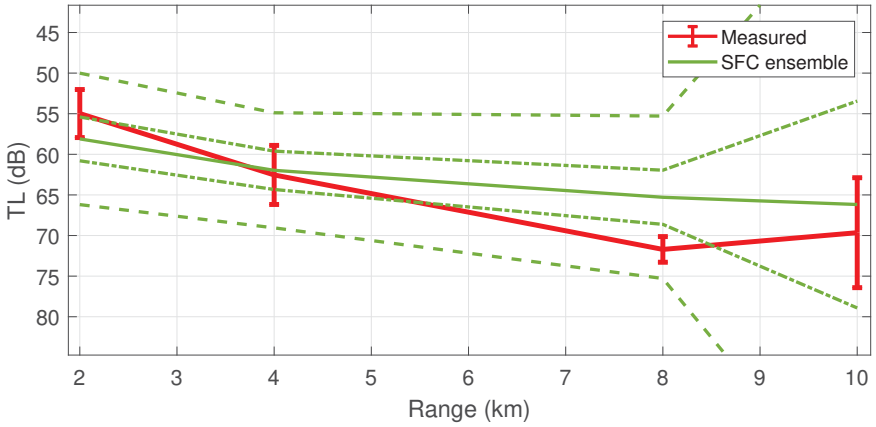

Figure 6.7: TL comparison between measured data with errorbars representing 3 standard deviations (red) and rough surface ensemble (green) with 1 (dash-dot line) and 3 (dashed line) standard deviations.

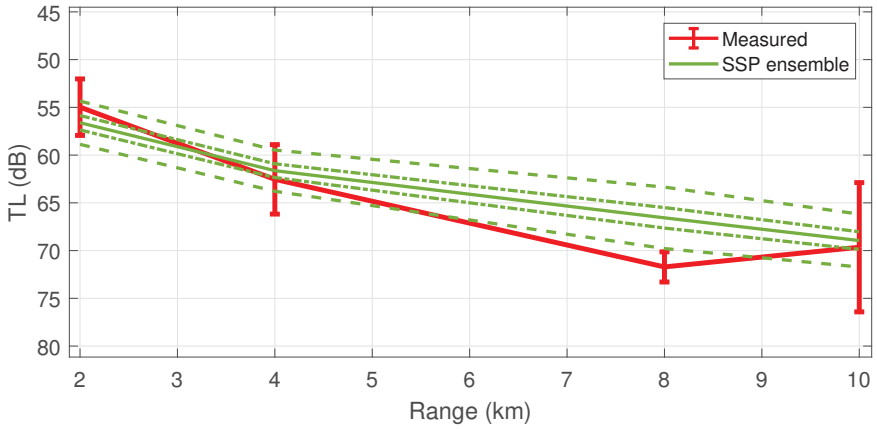

Figure 6.8: TL comparison between measured data with errorbars (red) and SSP ensemble (green) with 1(dash-dot line) and 3 (dashed line) standard deviations.

The large TL deviation of the surface ensemble is mostly caused by the varying position of the receiver since the change in sea surface only caused deviations of less than 0.5 dB (ref. Table 6.5). Comparing to the spread between receivers observed in Figure 6.2, the simulated spread is approximately 2 times larger. This discrepancy could be due to the dimensions of the box misrepresenting the actual range of relative motion experienced during the sea trial, but this could not be verified due to the lack of instrumentation on the receiver. The main conclusion remains: the receiver's position has a significant impact on the TL. The spread observed in the SSPs ensemble is only slightly lower than the measurements and may therefore be a significant contributor to TL deviation.

With the exception of the 8 km range, the mean of both ensembles are within the observed TL spread. Also, the mean of the measured TL falls between 3 standard deviations for both ensembles. Therefore, both ensembles estimated the measured TL well.

The delay spread is the last performance metric to be compared. Tables 6.6 and 6.7 summarize the delay spreads obtained through signal processing and simulation. Similarly to the measurements, the simulations did not show delay spreads increasing as a function of range.

Ensemble/ Range	2 km	4 km	8 km	10 km
Surface	21	12	13	20
Sound Speed	49	38	23	32
Measured	15	23	38	18

Table 6.6: RMS delay spread mean as a function of ensemble and range in milliseconds.

Ensemble/ Range	2 km	4 km	8 km	10 km
Surface	5.6	12	4.3	21
Sound Speed	5.5	61	59	141
Measured	103	368	164	103

Table 6.7: RMS delay spread variance as a function of ensemble and range.

The observations made in section 4.2 are valid across all ranges. The delay spreads from the rough surface ensemble are always lower than those from the SSP ensemble. The simulated delay spreads are within a factor of 2 from the measured values and the variances are not representative of the measurements. This level of fidelity is sufficient to determine whether or not ISI is an issue.

6.3 Other considerations

The impact of air bubbles on the UWAC was investigated, but not incorporated into the simulations. In short, when wind speed reaches 6 m/s, the impact of surface bubbles becomes significant and affects the TL. This is especially true at frequencies above 4 kHz (Dol et al., 2013). Because the frequency used during the sea trials was 2 kHz and the wind speed was below 7 m/s for the entire trial, the impact of bubbles was omitted. The lost in fidelity is most likely negligible due to the limited number of ray interactions with the surface, but this is an area where the simulation could be improved upon.

Since one of the objectives was to quantify the contribution of each physical property on the UWAC variations, combining multiple varying parameters was not studied. The increase in complexity and computation time could be justified when trying to model the UWAC as such ensembles could provide a best and worst case scenario based on given physical properties and range of change expected during the transmission.

Particular attention was given to recreate environmental condition changes observed during the sea trial and as such, the contributions of those parameters are for this specific environment and setup, a shallow channel with relatively flat bottom and a downward refracting SSP with source and receiver in the middle of the water column.

Chapter 7

Conclusion

In this thesis results from an at sea underwater acoustic communication experiment were analyzed and compared to ray-tracing simulations to identify the sources of discrepancies between measurements and simulation outputs as well as to quantify the contributions of major physical properties to the overall time-variance of the channel. In this chapter a summary of the results is presented in Section 7.1. Section 7.2 adds some closing remarks.

7.1 Summary of contributions and results

This thesis had three main contributions. The first contribution was covered in Chapters 3 and 4, and it is to present the DalComms1 sea trial, the data collected and the analysis of the received signal. The rich data set contains CTD, ADCP, SPIRIT and localization data as well as a 9 min recordings from ranges between 2 km and 10 km. The TL observed fell between cylindrical and spherical spreading losses. At times, TL difference due to the spatial separation between the top and bottom receiver reached upwards of 10 dB. The delay spread is significant and most likely caused inter-symbol interference. Despite the high delay spread, the coherence time was much greater than the symbol period indicating that the channel can be considered as slowly fading. The inverse relationship between wind speed and coherence time is in agreement with other recent experiments discussed in section 2.6. Finally, the Doppler spread suggests that some relative motion exists between the source and receiver on a scale of a few cm/s. We were not able to collect horizontal motion data, but the ship's drift and the lack of stability at the source and receiver definitely induced motion. With all of the above factors considered, an estimate of 4 cm/s is realistic.

The second contribution was covered in chapter 5, and it is to compare the sea trial results to a ray-trace using Bellhop. It was shown that Bellhop produced an accurate TL when the amp-delay output was summed incoherently. Bellhop was

used to obtain a CIR and it reproduced the 3 strongest arrivals with fidelity.

The final contribution was to quantify the contributions of the main physical properties to the time-variance of the UWAC. For this purpose, results from 3 ensembles with varying rough surface realizations, SSPs and bottom properties (attenuation and sound speed) were analyzed. In this thesis, the impact of the changing sea surface was minimal and lead to deviations of less than 0.5 dB. Changes in sound speed had a significant impact on TL deviations and led to a spread of 7 dB. The position of the receiver within a 9x5 m box was the greatest contributor to TL variance with a spread of more than 10 dB which is in line with the variance seen between receivers on the VLA. Error in bottom properties estimation affects the TL, but to a lesser extent. The ensembles were also used to estimate the delay spread and the results were within a factor of 2 from the measurements which was accurate enough to assess the possibility of ISI.

In light of the results and findings presented in the preceding sections, we can conclude that:

1. Findings from recent experiments, such as the relation between wind speed and coherence time, and the impact of SSP variation on TL were observed with the DalComms1 data set.

2. When combined with an estimated or historical range of variation in physical properties, a series of Bellhop simulations can be a good estimator of the mean or deterministic solution, and can also capture most of the variance induced by the time-variant environment.

3. SSP and receiver's motion/position were the largest contributors to TL deviations and their monitoring is important when trying to reproduce experiment results. The deviation caused by the position/motion of the receiver matched the deviation observed between both ends of the VLA. Additionally, the deviation generated by the SSP variation was accounting for the majority of the time-variance seen in the measurements.

7.2 Closing remarks

DalComms1 sea trial generated a substantial data set which includes concurrent environmental and underwater acoustic communication data. Channel estimation theory was used to extract performance metrics such as estimated CIR, Doppler and delay spread, and coherence time. Thereafter, Bellhop was used to reproduce the sea trial environment with the objective to find similar results. The deterministic solution provided by Bellhop seems to be in agreement with the large timescale, or averaged, results obtained from the sea trial measurements. The dominant tap arrivals and their respective delays simulated through Bellhop are representative of channel estimation obtained with the probing sequence. It is also evident that some discrepancies remained and that augmenting the ray-tracing solution with a statistical model contribution would improve its fidelity. As a stepping stone, a series of simulation ensembles with varying physical parameters was analyzed to determine the UWAC's sensitivity to a variety of environmental perturbations. Results were compared to sea trial measurements and showed reasonable agreement. Lastly, results illustrated the importance of high quality SSP and position data collection to accurately simulate the UWAC using a ray-tracing model.

Bibliography

Akyildiz, I. F., D. Pompili, and T. Melodia (2004). Challenges for efficient communication in underwater acoustic sensor networks. *ACM SIGBED Review 1*(2), 3–8.

Akyildiz, I. F., D. Pompili, and T. Melodia (2005). Underwater acoustic sensor networks: Research challenges. *Ad Hoc Networks 3*(3), 257–279.

Badiey, M., Y. Mu, J. A. Simmen, and S. E. Forsythe (2000). Signal Variability in Shallow-Water Sound Channels. *IEEE Journal of Oceanic Engineering 25*(4), 492–500.

Campos, L. (1986). On linear and non-linear wave equations for the acoustics of high-speed potential flows. *Journal of Sound and Vibration 110*(1), 41–57.

Carbone, N. M. and W. S. Hodgkiss (2000). Effects of Tidally Driven Temperature Fluctuations on Shallow-Water Acoustic Communications at 18 kHz. *IEEE Journal of Oceanic Engineering 25*(1), 84–94.

Chen, C. and F. J. Millero (1977). Speed of sound in seawater at high pressures. *The Journal of the Acoustical Society of America 62*(5), 1129–1135.

Dol, H. S., M. E. Colin, M. Ainslie, F. Gerdes, A. Schäfke, and H. Ö. Sertlek (2013). Validation of Simulations of an Underwater Acoustic Communication Channel Characterized by Wind-Generated Surface Waves and Bubbles. *International Conference and Exhibition on Underwater Acoustics 38*(4), 449–456.

Domingo, M. C. (2008). Overview of channel models for underwater wireless communication networks. *Physical Communication 1*(3), 163–182.

Feyman, R., R. Leighton, and M. Sand (1969). *Lectures on Physics - Volume 1* (1st editon ed.). Addison Wesley.

Fisher, F. H. and V. P. Simmons (1977). Sound absorption in sea water. *The Journal of the Acoustical Society of America 62*(3), 558–564.

Fofonoff, N. P. and R. C. Millard (1983). Algorithms for computation of fundamental properties of seawater. *UNESCO Technical papers in marine science 44*, 1–53.

Francois, R. E. and G. R. Garrison (1982). Sound absorption based on ocean measurements. Part II: Boric acid contribution and equation for total absorption. *The Journal of the Acoustical Society of America 72*(6), 1879–1890.

Hamilton, E. (1970). Sound velocity and related properties of marine sediments. *Journal of Geophysical Research 75*(23), 4423–4446.

Hamm, C., S. Blouin, and M. Taillefer (2015). Toward hardware-driven simulation of underwater acoustic propagation and communication with Arctic ice, wind waves, and currents. *OCEANS'15 MTS/IEEE Washington*, 1–6.

Jensen, F. B., W. A. Kuperman, M. B. Porter, and H. Schmidt (2000). *Computational Ocean Acoustics*. Springer Science & Business Media.

Kilfoyle, D. B. and A. B. Baggeroer (2000). The State of the Art in Underwater Acoustic Telemetry. *IEEE Journal of Oceanic Engineering 25*(1), 4–27.

Mackenzie, K. V. (1998). Nine-term equation for sound speed in the oceans. *The Journal of the Acoustical Society of America 70*(3), 807–812.

NOAA. (Aug. 16, 2017). National Oceanic and Atmospheric Administration. [Online]. Available: http://www.noaa.gov/.

Novosel, L. and G. Si (2014). Comparison of pseudo noise sequence lengths for a correlator channel sounder. In *ELMAR (ELMAR), 2014 56th International Symposium, 2014 56th International Symposium*, Number September, pp. 139–142.

Pierson, J., J. Willard, and L. Moskowitz (1964). A proposed spectral form for fully developed wind seas based on the similarity theory of S.A. Kitaigorodskii. *Journal of Geophysical Research 69*(24), 5181–5190.

Porter, M. B. (2011). The BELLHOP manual and users guide: Preliminary draft. [Online]. Available: http://oalib.hlsresearch.com/Rays/HLS- 2010-1.pdf.

Porter, M. B. and H. P. Bucker (1987). Gaussian beam tracing for computing ocean acoustic fields. *Acoustical Society of America 82*(4), 1349–1359.

Qarabaqi, P. and M. Stojanovic (2009). Statistical Modeling of a Shallow Water Acoustic Communication Channel. In *Underwater Acoustic Measurements conference, Nafplion, Greece*, pp. 1341–1350.

Radosevic, A., J. G. Proakis, and H. Avenue (2009). Statistical Characterization and Capacity of Shallow Water Acoustic Channels. *IEEE Oceans 2009 - Europe*, 1–8.

Rappaport, T. S. (1996). *Wireless Communications, Principles and Practice* (vol. 2 ed.). New Jersey: Prentice Hall PTR.

Rodriguez, O. C. (2008). General Description of the Bellhop Ray Tracing Program. [Online]. Available: http://oalib.hlsresearch. com/Rays/GeneralDescription.pdf.

Song, A., M. Badiey, H. C. Song, W. S. Hodgkiss, M. B. Porter, and K. Group (2008). Impact of ocean variability on coherent underwater acoustic communications during the Kauai experiment (KauaiEx). *Acoustical Society of America 123*(2), 856–865.

Thorp, W. H. (1967). Analytic Description of the Low Frequency Attenuation Coefficient. *The Journal of the Acoustical Society of America 42*(1), 270.

Tomasi, B., G. Zappa, K. Mccoy, P. Casari, and M. Zorzi (2010). Experimental Study of the Space-Time Properties of Acoustic Channels for Underwater Communications. *IEEE Oceans 201*, 1–9.

Urick, R. (1983). *Principles of Underwater Sound* (3rd ed.). New York: McGraw-Hill.

Walree, P. V. (2011). Channel sounding for acoustic communications : techniques and shallow-water examples. *Norwegian Defence Research Establishment (FFI), Tech. Rep. FFI-rapport 7*, 1–58.

Wong, G. S. K. and S. Zhu (1995). Speed of sound in seawater as a function of salinity, temperature, and pressure. *The Journal of the Acoustical Society of America 97*(3), 1732–1736.

Yang, T. C. (2013). Properties of underwater acoustic communication channels in shallow water. *The Journal of the Acoustical Society of America 129*(2012), 129–145.

Appendix A: The UNESCO Equation for Sound Speed in Seawater

Original UNESCO equation as described in Fofonoff and Millard (1983) with coefficients recalculated by Wong and Zhu (1995) after the adoption of the International Temperature Scale of 1990.

$$c(S,T,P) = C_w(T,P) + A(T,P)S + B(T,P)S^{3/2} + D(T,P)S^2$$

$$\begin{aligned} C_w(T,P) =& (C_{00} + C_{01}T + C_{02}T^2 + C_{03}t^3 + C_{04}t^4 + C_{05}T^5) + \\ & (C_{10} + C_{11}T + C_{12}T^2 + C_{13}T^3 + C_{14}T^4)P + \\ & (C_{20} + C_{21}T + C_{22}T^2 + C_{23}T^3 + C_{24}T^4)P^2 + \\ & (C_{30} + C_{31}T + C_{32}T^2)P^3 \end{aligned}$$

$$\begin{aligned} A(T,P) =& (A_{00} + A_{01}T + A_{02}T^2 + A_{03}t^3 + A_{04}t^4) + \\ & (A_{10} + A_{11}T + A_{12}T^2 + A_{13}T^3 + A_{14}T^4)P + \\ & (A_{20} + A_{21}T + A_{22}T^2 + A_{23}T^3)P^2 + \\ & (A_{30} + A_{31}T + A_{32}T^2)P^3 \end{aligned}$$

$$B(T,P) = B_{00} + B_{01}T + (B_{10} + B_{11}T)P$$

$$D(T,P) = D_{00} + D_{10}P$$

Where

T = Temperature in degrees Celsius

S = Salinity in Practical Salinity Units

P = Water pressure in bars

Table of revised coefficients for UNESCO equation.

Coefficients	Value	Coefficients	Value
C_{00}	1402.388	A_{02}	7.166E-5
C_{01}	5.03830	A_{03}	2.008E-6
C_{02}	-5.81090E-2	A_{04}	-3.21E-8
C_{03}	3.3432E-4	A_{10}	9.4742E-5
C_{04}	-1.47797E-6	A_{11}	-1.2583E-5
C_{05}	3.1419E-9	A_{12}	-6.4928E-8
C_{10}	0.153563	A_{13}	1.0515E-8
C_{11}	6.8999E-4	A_{14}	-2.0142E-10
C_{12}	-8.1829E-6	A_{20}	-3.9064E-7
C_{13}	1.3632E-7	A_{21}	9.1061E-9
C_{14}	-6.1260E-10	A_{22}	-1.6009E-10
C_{20}	3.1260E-5	A_{23}	7.994E-12
C_{21}	-1.7111E-6	A_{30}	1.100E-10
C_{22}	2.5986E-8	A_{31}	6.651E-12
C_{23}	-2.5353E-10	A_{32}	-3.391E-13
C_{24}	1.0415E-12	B_{00}	-1.922E-2
C_{30}	-9.7729E-9	B_{01}	-4.42E-5
C_{31}	3.8513E-10	B_{10}	7.3637E-5
C_{32}	-2.3654E-12	B_{11}	1.7950E-7
A_{00}	1.389	D_{00}	1.727E-3
A_{01}	-1.26E-2	D_{10}	-7.9836E-6